Remote Sensing of Environment 246 (2020) 111884

Contents lists available at ScienceDirect

Remote Sensing of Environment

journal homepage: www.elsevier.com/locate/rse

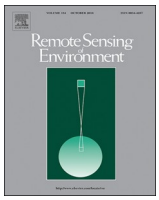

Cirrus clouds that adversely affect Landsat 8 images: What are they and how to detect them?

Shi Qiu[a,*], Zhe Zhu[a], Curtis E. Woodcock[b]

[a] Department of Natural Resources and the Environment, University of Connecticut, Storrs, CT 06269, USA
[b] Department of Earth and Environment, Boston University, Boston, MA 02215, USA

ARTICLE INFO

Keywords:
Landsat 8
Time series
Cirrus cloud detection
Cmask
Water vapor

ABSTRACT

We developed an algorithm called Cmask (Cirrus cloud mask) for cirrus cloud detection in Landsat 8 imagery using time series of Cirrus Band (1.36–1.39 μm) observations. For each pixel, a harmonic model, which includes a water vapor regressor, based on all available Cirrus Band observations is estimated using the Robust Iteratively Reweighted Least Squares (RIRLS) regression approach, and pixels affected by cirrus cloud are identified by comparing model predictions and actual satellite observations of the Cirrus Band Top-Of-Atmosphere (TOA) reflectance. Furthermore, we analyzed the effect of increasing Cirrus Band TOA reflectance on the surface reflectance of the Blue, Green, Red, Near Infrared (NIR), and two Shortwave Infrared (SWIR) (SWIR 1 and SWIR 2) Bands based on a set of globally distributed random samples. The goal of this study is to answer the question of what are cirrus clouds in the context of a Landsat observation, or more specifically, when should we identify a pixel as cirrus cloud such that we know the reflectance in the other spectral bands has been seriously affected by cirrus clouds. The challenge is to then develop a simple and operational algorithm for accurate detection of cirrus clouds in Landsat 8 images. The Cmask algorithm reduced almost by half the errors found in the U.S. Geological Survey (USGS) Quality Assessment (QA) Band for distinguishing cirrus cloud and clear observations (8% versus 15% error).

1. Introduction

As one of the most successful Earth Observation (EO) programs, the Landsat Program has made an enormous contribution to the science and applications of satellite remote sensing (Wulder et al., 2019), and its open and free data policy has benefited many aspects of the science community and beyond (Woodcock et al., 2008; Zhu et al., 2019). For example, the use of dense Landsat Time Series (LTS) for applications such as land cover change and land cover mapping at 30-m spatial resolution has been made possible for the first time (Brown et al., 2019; Hansen et al., 2013; Huang et al., 2010a; Kennedy et al., 2010; Pekel et al., 2016; Zhu and Woodcock, 2014a). Nevertheless, LTS contains a variety of sources of noise, which reduce the data consistency and make time series analysis difficult (Qiu et al., 2019a). Clouds are the major source of noise in LTS, and accurate detection of them is considered essential for time series analysis (Zhu et al., 2018).

Generally, clouds can be divided into three major categories: cumulus, stratus, and cirrus. Cumulus and stratus clouds are relatively easy to detect in Landsat imagery because of their high reflectance, white color, and cold temperature (Chai et al., 2019; Huang et al., 2010b; Irish et al., 2006; Zhu and Woodcock, 2012, 2014b). On the other hand, cirrus clouds, defined as "detached clouds in the form of white, delicate filaments, or white or mostly white patches, that are composed of ice crystals" (Huschke, 1970), are much more difficult to detect in remote sensing imagery. We are unaware of an algorithm that can provide accurate masks of cirrus clouds. It is also important to note that cirrus clouds have multiple types, which include cirrus, cirrostratus, and cirrocumulus (Heymsfield et al., 2016), as well as contrails (aircraft wake) (Burkhardt and Kärcher, 2011).

Cirrus clouds are hard to detect mainly because they are sometimes transparent or semi-transparent in the optical bands (Fig. 1a), even though they can actually have a substantial impact on the satellite observations, and have serious implications for their use in time-series applications such as change detection (Holden and Woodcock, 2016; Huang et al., 2010b). To help identifying cirrus clouds with high accuracy, Landsat 8 included a new Cirrus Band (Band 9) on the Operational Land Imager (OLI). This Cirrus Band is in the 1.36–1.39 μm wavelengths, which has a strong water vapor absorption feature (Gao et al., 1993, 2003). Normally, the water vapor in the atmosphere is sufficient to absorb most of the solar radiation at these wavelengths on

* Corresponding author.
E-mail address: shi.qiu@uconn.edu (S. Qiu).

https://doi.org/10.1016/j.rse.2020.111884
Received 10 September 2019; Received in revised form 7 May 2020; Accepted 9 May 2020
Available online 26 May 2020

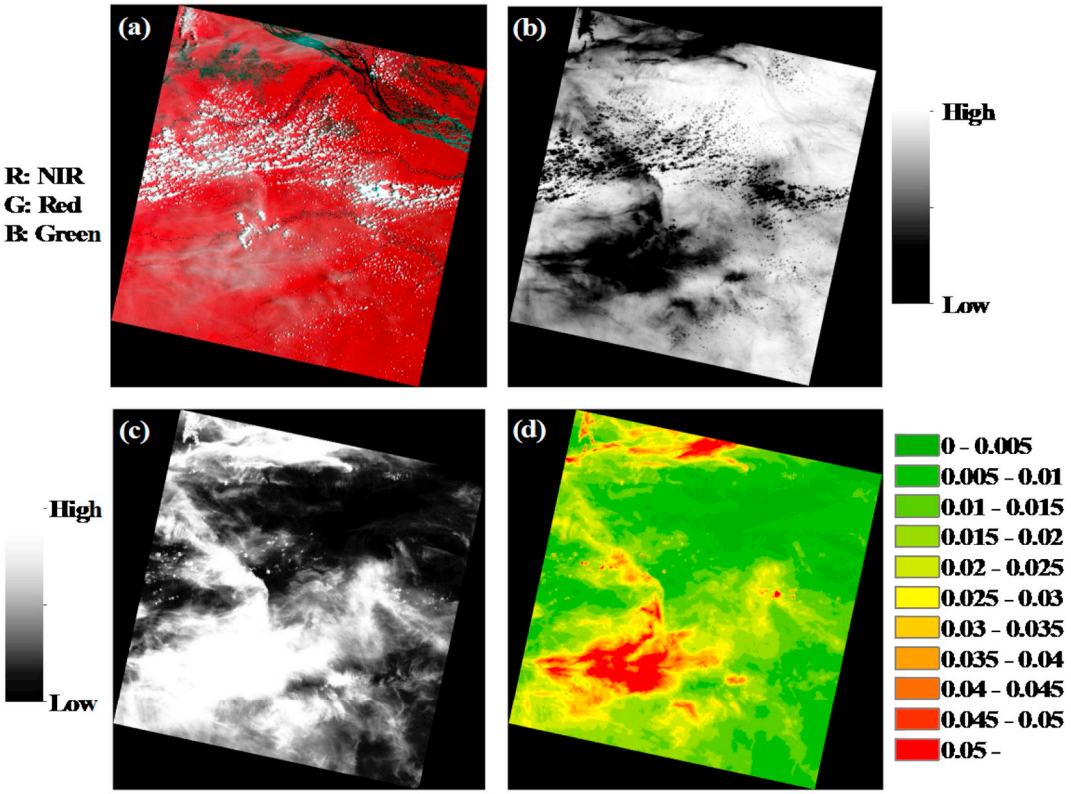

Fig. 1. An example illustrating that cirrus clouds are hard to identify in Landsat 8 images. (a) False color image (NIR, Red, and Green Bands). (b) Brightness Temperature. (c) Cirrus Band TOA reflectance. (d) Density slice of the same Cirrus Band. The image is located at Path 233/Row 61 acquired on October 5, 2013. (For interpretation of the references to color in this figure legend, the reader is referred to the web version of this article.)

the path from the sun to the surface to the sensor, making areas without cirrus clouds appear dark in the Cirrus Band (see black areas in Fig. 1c). However, cirrus clouds occur at high levels in the atmosphere, and reflected radiation from the top of cirrus clouds has a very short path through the atmosphere and hence the normal effect of water vapor absorption is greatly reduced. As a result, cirrus clouds appear bright in the Landsat 8 Cirrus Band (see white areas in Fig. 1c), making it particularly helpful for identifying cirrus clouds.

The atmospheric water absorption wavelengths (1.36–1.39 μm) have been used in Band 26 of the Moderate Resolution Imaging Spectroradiometer (MODIS) to detect cirrus clouds for decades. Gao et al. (2003) suggested that this special band is useful for identifying cirrus clouds even over polar regions where the atmosphere is extremely dry. They found that a threshold of 0.02 in MODIS Band 26 Top-Of-Atmosphere (TOA) reflectance can identify thick cirrus clouds, even over the polar regions. However, the use of this threshold may miss some thin cirrus clouds. The algorithm for generating the MODIS cloud mask product (MOD35) also has a cirrus cloud detection component (Ackerman et al., 1998; King et al., 2003; Platnick et al., 2003), in which cirrus clouds are detected based on different rules for snow covered and non-snow covered places separately. Three confident levels are provided for the cirrus cloud quality assessment bits, in which a threshold of 0.04 in MODIS Band 26 indicates high confidence of detection, 0.035 for middle confidence, and 0.03 for low confidence over places without snow; and 0.06 for high, 0.0525 for middle, and 0.045 for low confident cirrus clouds over snow (Frey et al., 2008). Note that the relatively high thresholds used in the MOD35 product are partially because of the electronic "cross-talk" problem in MODIS Band 26, which creates noise that might be confused with cirrus clouds at lower thresholds (Guenther et al., 2002). Fortunately, the Landsat 8 Cirrus Band does not have this artifact, and a lower threshold is possible to better capture thin cirrus clouds without committing large commission errors from the "cross-talk" noise. Wilson and Oreopoulos (2013) proposed an enhanced algorithm for detecting clouds in Landsat 8 imagery by following the several spectral tests designed for MODIS data proposed by Luo et al. (2008), and added a threshold of 0.0113 in the Cirrus Band to identify cirrus clouds. Similarly, the U.S. Geological Survey (USGS) generates a cirrus cloud Quality Assessment (QA) in Landsat 8 imagery based on a fixed global threshold of 0.02 (Kovalskyy and Roy, 2015). The threshold can identify most of the cirrus clouds, but will also persistently misclassify land surfaces in dry environments or at high altitudes that reflect strongly in these wavelengths similar to cirrus clouds. Zhu et al. (2015a) expanded the Function of mask (Fmask) algorithm originally designed for Landsats 4–7 images (Zhu and Woodcock, 2012) to improve cloud detection in Landsat 8 imagery by adding a new cirrus cloud probability based on the Cirrus Band. The Fmask results have been significantly improved for thin cirrus clouds, but they may misidentify high elevation sites as clouds where the Cirrus Band is also very bright. To reduce the effect of high elevation surfaces on Cirrus Band, Qiu et al. (2019b) recently proposed Version 4.0 of Fmask to enhance the cloud detection for Landsat data by integrating a Digital Elevation Model (DEM) to normalize the Cirrus Band. However, omission and commission errors of cirrus clouds were still observed.

Cirrus clouds are abundant in the atmosphere (Sassen et al., 2008). Kovalskyy and Roy (2015) estimated that approximately 28% of Landsat 8 data across the conterminous United States (CONUS) are contaminated by cirrus clouds. It is obvious that a good cirrus cloud detection algorithm is of high interest, but in the remote sensing community there is no unanimous agreement on what constitutes a cirrus cloud in remotely sensed imagery, or a quantitative definition of what the effect of a cirrus cloud has to be such that it merits removal from future analyses. For example, in Fig. 1d, it is difficult to find an optimal threshold for creating a cirrus cloud mask (especially for the ranges between the green and yellow colors), and this creates major

challenges for efforts to evaluate the performance of cirrus cloud detection algorithms because each interpreter may have their own visual thresholds for identifying cirrus clouds (which may even change when the image is stretched differently). Therefore, in this study, we quantitatively defined a "cirrus cloud" in Landsat 8 imagery by analyzing their effect on the surface reflectance products of other spectral bands, and at the same time developed a new algorithm for providing Cirrus cloud mask (Cmask) based on a time series of values in the Landsat 8 Cirrus Band.

2. Data

The basis for Cmask is to predict what the reflectance would be for individual pixels in a Landsat 8 image if cirrus clouds were not present at the time the observations were collected. The basis for those predictions is past observations and the atmospheric conditions, i.e. the water vapor content, at the time of image acquisition. Therefore, two major inputs were included in this analysis: Integrated Water Vapor (IWV) provided by the second Modern-Era Retrospective analysis for Research and Applications (MERRA-2) and cirrus band time series provided by Landsat 8.

2.1. Integrated water vapor

The IWV data are derived from MERRA-2 by the National Aeronautics and Space Administration (NASA) Global Modeling and Assimilation Office (GMAO) (GMAO, 2015). The MERRA-2 product is generated using Version 5.12.4 of Goddard Earth Observing System (GEOS) atmospheric model, that combines surface and satellite observations, such as Advanced Very High Resolution Radiometer (AVHRR), Special Sensor Microwave Imager/Sounder (SSMIS), and MetOp-A Advanced Scatterometer (ASCAT), to generate products such as atmospheric IWV (Gelaro et al., 2017). The IWV product is provided hourly at a resolution of 0.625° × 0.5° globally. The Cmask algorithm acquires the hourly water vapor data corresponding to the acquisition time of each Landsat 8 image (derived from Landsat metadata) and resamples it to match Landsat pixels at 30-m resolution using a nearest resampling approach. The IWV data help Cmask to capture the variability caused by sudden changes of the atmospheric water vapor content, especially for places with dry air such as high mountains and polar ice/snow sheets (see Section 4.1 for details). Note that as atmosphere change often occurs at a large scale, the disagreement of the spatial resolutions between Landsat 8 data and IWV data will have limited effect on the final results.

2.2. Landsat 8 data

To quantify the effects of cirrus cloud on surface reflectance and develop the Cmask algorithm, a total of 24 Landsat 8 scenes in Worldwide Reference System two (WRS-2) were collected around the world by following the sites of "L8 Biome". The "L8 Biome" is a cloud cover assessment dataset designed for Landsat 8 that is stratified by biome (Foga et al., 2017). It covers eight different land cover types, such as urban, barren, forest, shrubland, grass/cropland, snow/ice, wetlands, and water; and within each cover type, there are a total of 12 different Landsat WRS-2 scenes. In this study, we selected a total of 24 scenes covering different land cover types from different parts of the world from the "L8 Biome" datasets, with three sites randomly selected from each cover type (Fig. 2; Table S1). In each scene, we downloaded all available Landsat 8 Collection 1 Level-2 data (USGS, 2014) between

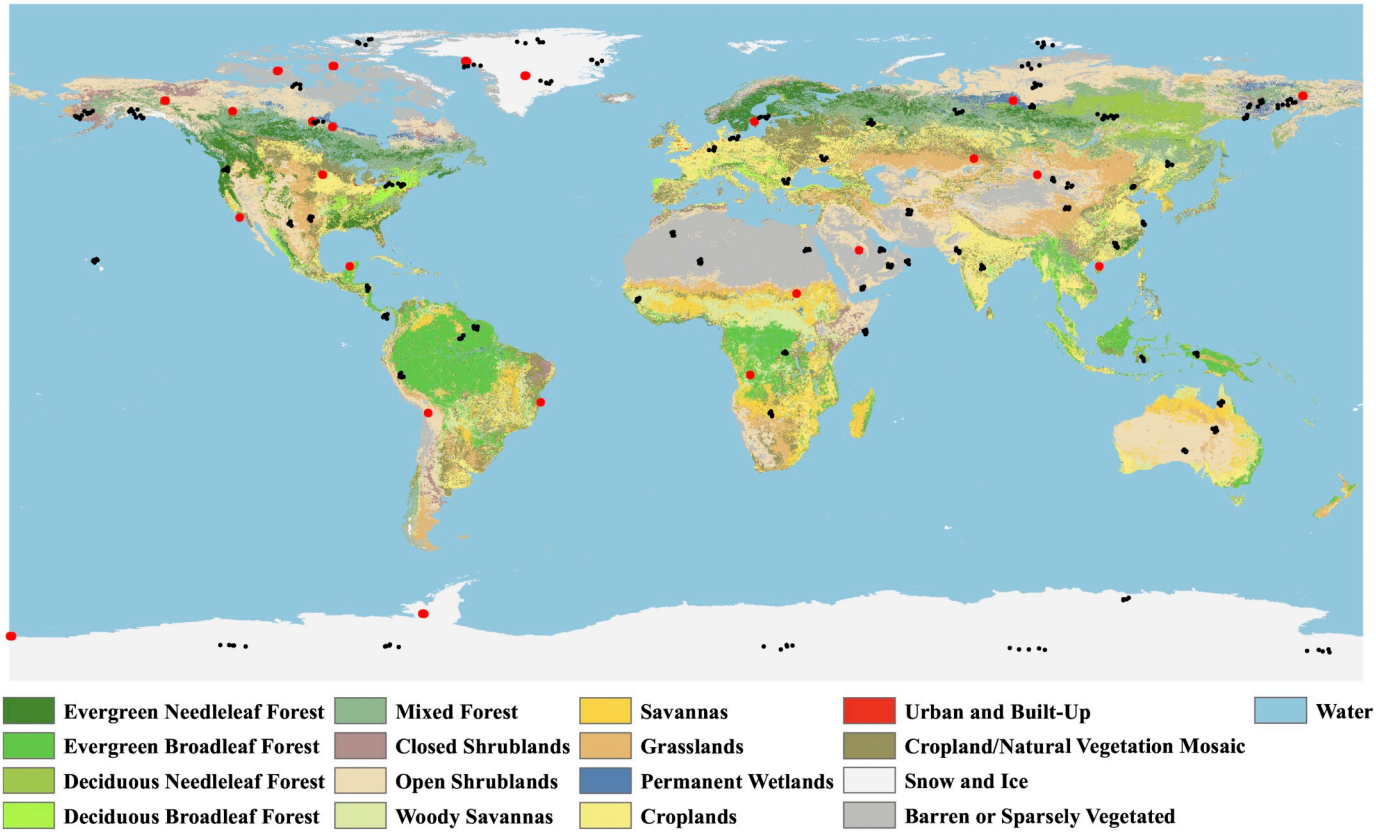

Fig. 2. Distribution of Landsat 8 data used in this study. The red points indicate the locations of Landsat 8 scenes used for quantifying effects of cirrus clouds and training the Cmask algorithm (500 pixels × 500 pixels), and the black points are the reference samples (pixels) used for accuracy assessment. The background land cover map is derived from the Global Land Cover Characterization (GLCC) product (Loveland et al., 2000). (For interpretation of the references to color in this figure legend, the reader is referred to the web version of this article.)

March 2013 to June 2018 over a central subset of 500 pixels × 500 pixels from Earth Resources Observation and Science (EROS) Center Science Processing Architecture (ESPA; https://espa.cr.usgs.gov; Last access on January 10, 2020), including surface reflectance, TOA reflectance, and QA. This gave us a total of 2169 Landsat 8 subset images. The surface reflectance is generated using the Landsat 8 Surface Reflectance Code (LaSRC) developed by Vermote et al. (2016). Note that some images were excluded from our analysis because when their solar zenith angles are larger than 76 degrees, they were not processed to surface reflectance. The QA Band has a cirrus cloud mask indicator using a simple 0.02 threshold in the Cirrus Band TOA reflectance (Kovalskyy and Roy, 2015). It also includes a cloud mask made using Fmask (including all kinds of clouds), which is created based on Version 3.3 of the Fmask algorithm (Zhu et al., 2015a; Zhu and Woodcock, 2012).

From the 2169 Landsat 8 subset images, we selected 303 with almost no cloud cover (fully clear images) and 122 that are almost completely covered by cirrus clouds (fully covered by cirrus clouds) to provide a sufficient number of observations to help determine the key parameters in Cmask (Table S2 and S3). We interpreted the entire images (fully clear or fully covered by cirrus clouds) rather than single pixels, as cirrus clouds often occur over large areas and a one-time large-scale interpretation can provide lots of samples.

To evaluate the accuracy of the Cmask algorithm, we carefully interpreted another 1800 reference samples based on a simple random strategy, in which 5 pixels were randomly selected from each of the remaining 72 Landsat 8 sites of the “Biome” dataset, and for each pixel, 5 observations were randomly selected from the entire Landsat 8 time series (Fig. 2). Three categories, ‘cirrus cloud’, ‘non-cirrus cloud’ (i.e. another kind of cloud), and ‘clear’, were carefully determined by the spectral, shape, and texture characteristics from the Landsat 8 imagery. If a pixel is bright in the Cirrus Band and presents any of the cirrus cloud shape/texture properties in Table 1, it will be interpreted as ‘cirrus cloud’; otherwise, it is labeled as either ‘non-cirrus cloud’ or ‘clear’. Sometimes it is hard to determine the category for some samples (e.g., cirrus or non-cirrus cloud). We excluded a small proportion of samples that are difficult to interpret, and a total of 1722 reference samples were collected (Table 1). The reference samples can be found at www.github.com/gersl/cmask.

3. Effect of cirrus cloud on optical spectral bands

To identify the optimum threshold for cirrus cloud detection using the Cirrus Band, we analyzed the effect of increments of the Cirrus Band TOA reflectance on the surface reflectance of six optical bands (Band 2 - Blue, Band 3 - Green, Band 4 - Red, Band 5 - NIR, Band 6 - SWIR1, and Band 7 - SWIR2) in Landsat 8. We define an observation to have been affected by a cirrus cloud if the cloud's presence has caused the change of any of the six optical bands larger than two times the estimated overall uncertainty from the LaSRC atmospheric correction algorithm (Vermote et al., 2016). Assuming the uncertainty from the LaSRC atmospheric correction algorithm follows a normal distribution, the use of two times the uncertainty for defining observations affected by cirrus clouds maintains similar uncertainty as Landsat 8 surface reflectance (within 95% confidence interval).

To estimate the increment of the Cirrus Band TOA reflectance caused by cirrus cloud, we need to predict Cirrus Band TOA reflectance for observations not affected by cirrus cloud. This step is necessary, as in some locations and situations, surface reflectance contributes to the observed TOA reflectance in the Cirrus Band, and unless we account for this contribution by the surface, we won't be able to separate it from the effect of the clouds. We developed a time series model to perform this task (see Section 4 for details), and by differencing the predicted TOA reflectance with the observed TOA reflectance in the Cirrus Band, we can estimate how much the Cirrus Band TOA reflectance increases. The larger the difference, the more likely the observation is adversely affected by a cirrus cloud.

We also estimated the surface reflectance of the six optical bands for clear observations. We used the Continuous Change Detection and Classification (CCDC) algorithm to predict the surface reflectance of each optical band for the corresponding observations (Zhu et al., 2015b). The CCDC algorithm uses clear observations, derived from the Fmask and Tmask (multiTemporal mask) algorithms (Zhu et al., 2015a; Zhu and Woodcock, 2012, 2014b), to predict the surface reflectance at any given date. Meanwhile, it also detects land cover changes by continually differencing the CCDC predictions and the actual observations in the optical bands. In this study, we only used stable pixels (no land cover change) for our analysis because the change detection results are not 100% accurate and errors may affect prediction of surface

Table 1
Cloud categories and the number of samples collected within each category.

Types		Number of Samples	Definitions
Cirrus cloud	Cirrus	460	Detached clouds in the form of white, delicate filaments, mostly white patches or narrow bands. They may have a fibrous (hair-like) and/or silky sheen appearance.
	Cirrostratus		Transparent, whitish veil clouds with a fibrous (hair-like) or smooth appearance. A sheet of cirrostratus which is very extensive, nearly always ends by covering the whole sky.
	Cirrocumulus		Thin, white patch, sheet, or layered of clouds without shading. They are composed of very small elements in the form of more or less regularly arranged grains or ripples. There will be a connection with cirrus or cirrostratus and will show some characteristics of ice crystal clouds.
	Contrails		Narrow, elongated cloud formed as jet aircraft exhaust condenses in cold air at high altitudes, indicative of upper level humidity and wind drift.
Non-cirrus	Non-cirrus cloud	386	Any cloud type, except for cirrus clouds.
	Clear	876	Observations without any kinds of clouds.

Definitions are from U.S. National Weather Service (NWS) (https://www.weather.gov; Last access on January 10, 2020).

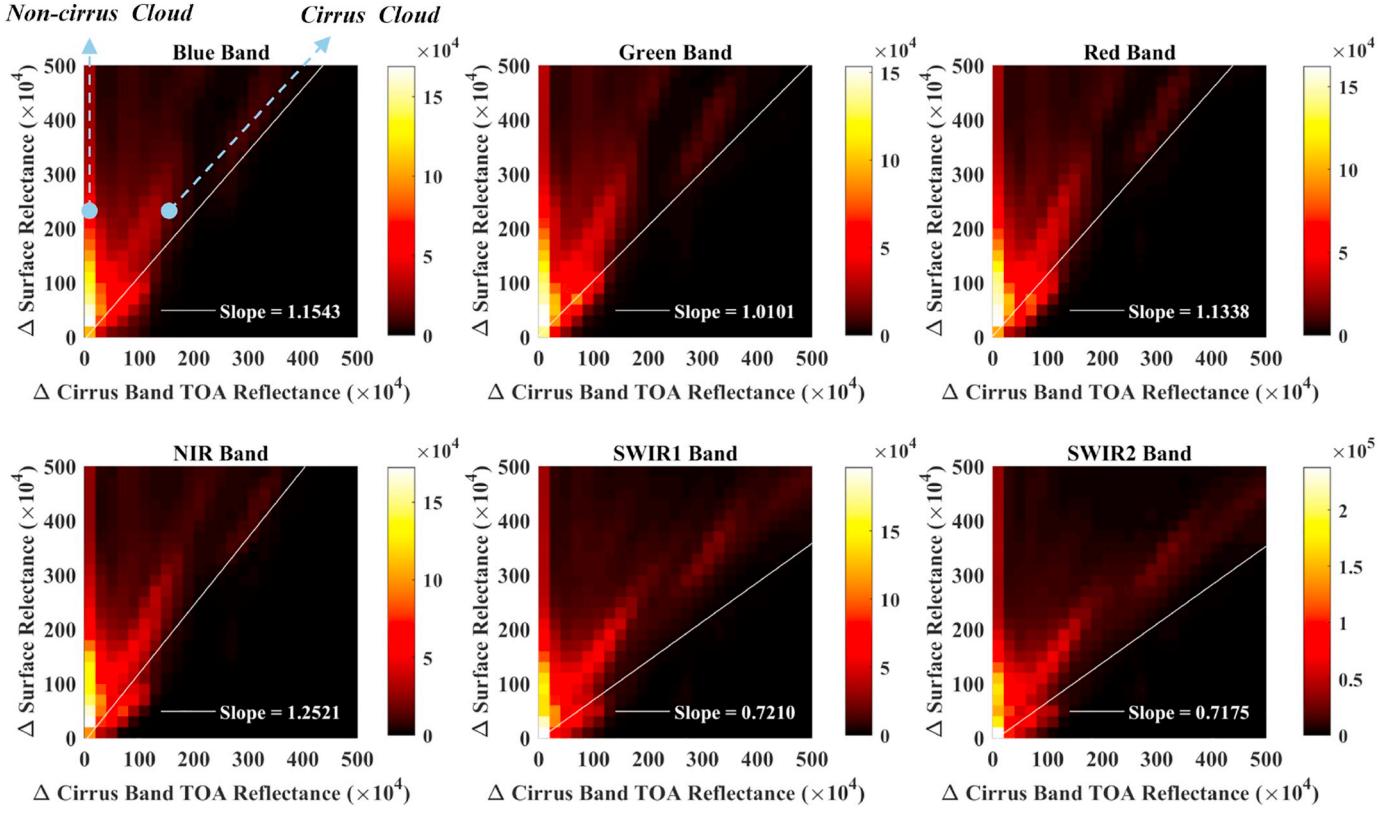

Fig. 3. Scatter plots of the increment of the surface reflectance of Blue, Green, Red, NIR, SWIR1, and SWIR2 Bands versus the increment of the Cirrus Band TOA reflectance based on the dark surface samples (CCDC predicted surface reflectance less than 0.1) derived from 2169 Landsat 8 images globally distributed over 24 sites (Fig. 2). Δ Cirrus Band TOA reflectance is the difference in Cirrus Band TOA reflectance between the real observation and the Cmask prediction, and Δ surface reflectance is the difference of surface reflectance between the real observation and the CCDC prediction for each of the spectral bands. The white line is the estimated Cirrus Line (CL). (For interpretation of the references to color in this figure legend, the reader is referred to the web version of this article.)

reflectance. Moreover, considering that the bright land surfaces already have a high reflectance in each optical band and their surface reflectance may not change much even when cirrus clouds are present, we used all the stable observations where the predicted surface reflectance of all bands is less than 0.1 for our analysis (dark surface samples).

From the 2169 Landsat 8 subset images (Fig. 2), we randomly selected 0.1% (for reducing computation) of the dark surface pixel samples (with CCDC predicted surface reflectance less than 0.1) and plotted the increment (real observation – Cmask prediction) of Cirrus Band TOA reflectance versus the increment (real observation – CCDC prediction) of surface reflectance for Blue, Green, Red, NIR, SWIR1, and SWIR2 Bands, respectively (Fig. 3). In each plot, a bimodal pattern can be observed, that presents non-cirrus cloud and cirrus cloud characterization (as the example for the Blue Band in Fig. 3). Non-cirrus clouds (e.g., cumulus and stratus) are usually at low altitudes and optically thick, and subsequently they hardly vary in Cirrus Band TOA reflectance (which is always dark) but often increase the reflectance surface of optical bands substantially. Therefore, they often are piled-up near the y-axis (little or no difference in Cirrus Band but large difference in other bands). On the other hand, cirrus clouds are often at high altitudes (most likely in 8.5– 10 km range) and most cirrus clouds are optically transparent or semi-transparent with different optical depths (Mace et al., 2001). It is well understood that the thinner the cirrus cloud, the less its impact on observations in optical bands. Therefore, the bottom line of the scatter plot shows the impact of cirrus clouds with the least optical thickness, which is also the kind of "invisible" cirrus clouds that are most difficult to detect. To better capture this bottom line within each scatter plot, we used Ordinarily Least Squares (OLS) regression to generate a straight line against the low statistical value (two percentile) of surface reflectance difference within each 0.002 interval of the Cirrus Band TOA reflectance difference (see white lines in Fig. 3). This straight line is considered as the "Cirrus Line" (CL), which quantifies the impacts of most thin cirrus clouds on surface reflectance of different optical bands. It is worth noting that the use of the low statistical value (two percentile) can exclude potential outliers from the band-to-band misalignments of clouds caused by the parallax effect of the OLI focal plane (Gao and Li, 2017), as cloud displacement pixels will mainly locate in the areas close to the x-axis (large difference in Cirrus Band but less difference in other bands) or y-axis (little or no difference in Cirrus Band but large difference in other bands) in Fig. 3.

Based on the CLs and the allowed uncertainty of surface reflectance, we can estimate a threshold for cirrus cloud detection based on the

Table 2
Selection of cirrus cloud thresholds according to the uncertainty of the Landsat 8 OLI surface reflectance from the LaSRC algorithm (Vermote et al., 2016).

OLI band	Wavelength (μm)	Slope	Surface reflectance uncertainty	Cirrus cloud threshold
Blue	0.452–0.512	1.1543	0.0085 (0.0170)	0.0147
Green	0.533–0.590	1.0101	0.0054 (0.0108)	0.0107
Red	0.636–0.673	1.1338	0.0040 (0.0080)	0.0071
NIR	0.851–0.879	1.2521	0.0026 (0.0052)	0.0042
SWIR 1	1.566–1.651	0.7210	0.0011 (0.0022)	***0.0031***
SWIR 2	2.107–2.294	0.7175	0.0036 (0.0072)	0.0100

Note the cirrus cloud thresholds are calculated based on two-times surface reflectance uncertainty of each band (the number in bracket). The minimum value of 0.0031 (highlighted in the bold and italic letter) is chosen as the optimum threshold to define cirrus cloud, which ensures all optical bands are within the threshold of twice the uncertainty of the surface reflectance products.

difference between observed and predicted cirrus band TOA reflectance. The results suggest that the cirrus cloud threshold is band-dependent and when the presence of cirrus clouds increases the Cirrus Band TOA reflectance between 0.0031 and 0.0147, they will affect at least one of the optical bands by more than double the uncertainty of the surface reflectance products (within 95% confidence interval) (Table 2). Therefore, a threshold of 0.0031 increase in Cirrus Band TOA reflectance is suggested for cirrus cloud detection to ensure all optical bands are within the threshold of twice the uncertainty of the surface reflectance products. Note that the threshold of 0.0031 is used for the Cirrus Band TOA difference between model prediction and actual observation, instead of applied directly on the Cirrus Band as other studies did (Kovalskyy and Roy, 2015; Wilson and Oreopoulos, 2013). The proposed cirrus cloud threshold is also much lower than has been proposed in other previous studies (usually between 0.02 and 0.04), which is mostly due to the better prediction of Cirrus Band TOA reflectance.

4. Detection of cirrus clouds – Cmask algorithm

Unlike most of the multitemporal cloud detection algorithms that use the optical bands acquired at a different time to identify clouds (Frantz et al., 2015; Goodwin et al., 2013; Hagolle et al., 2010; Zhu and Helmer, 2018; Zhu and Woodcock, 2014b), the Cmask algorithm uses only the Cirrus Band time series to identify cirrus clouds. The basic idea is that we can predict the Cirrus Band TOA reflectance of "non-cirrus" (or "good") observations at any date using a time series model. When the observed TOA reflectance of the Cirrus Band is higher than the model prediction, it is labeled as a cirrus cloud. The flowchart of the Cmask algorithm is illustrated in Fig. 4.

4.1. Cmask time series model

For every pixel, a harmonic time series model with a water vapor regressor will be estimated based on all Landsat 8 Cirrus Band observations. The Cirrus Band is a water vapor absorption band, which is sensitive to water vapor concentration in the atmosphere when no cirrus clouds are present. Water vapor can change dramatically from day to day, or even from hour to hour based on patterns of temperature and precipitation (Nilsson and Elgered, 2008). For most atmosphere conditions, there is sufficient water vapor to make the Cirrus Band extremely dark. Nevertheless, for areas with very dry atmospheres, the seasonal variation of water vapor (Mastenbrook, 1971) will ultimately affect the Cirrus Band, and sometimes make the land surface visible in the Cirrus Band. Therefore, we used a harmonic model (Davis, 1986; Rayner, 1971) to model the intra-annual change in the Cirrus Band TOA reflectance (Eq. (1)) for each pixel. However, the harmonic model alone cannot capture the sudden change of Cirrus Band TOA reflectance caused by the fluctuation of water vapor (e.g., dry air). Thus, we added

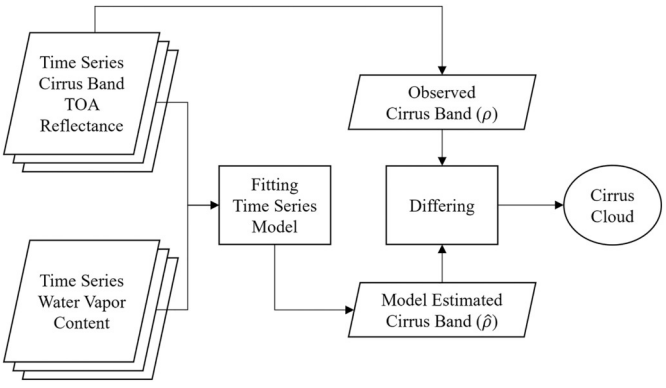

Fig. 4. Flowchart of Cmask algorithm.

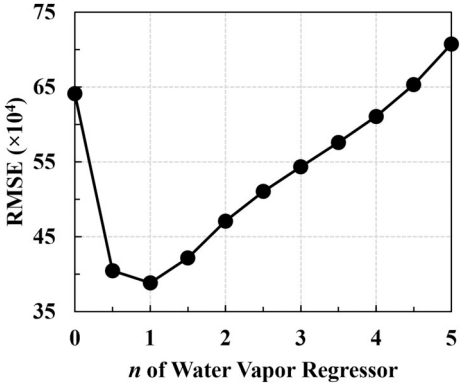

Fig. 5. Selection of n for the water vapor regressor using 303 absolutely clear images. Note that when n equals to 1, the model shows the lowest average Root Mean Square Error (RMSE). wv means integrated water vapor.

a water vapor regressor (provided from IWV) to account for the times when atmospheric water vapor differs from normal. According to the Beer-Lambert law, the water vapor absorption process in atmosphere can be described as an exponential function of the integrated water vapor content (wv), therefore, we added the water vapor regressor as shown in Eq. (1). To determine the optimum value of n, we changed n from 0 to 5 with an interval of 0.5, and evaluated model performance by calculating the average Root Mean Square Error (RMSE) between model estimates and real observations of the 303 clear images. When n equals to 1, the water vapor regressor (e^{-wv}) resulted in the highest accuracy (lowest RMSE) (Fig. 5). Note that exclusion of the water vapor regressor (when the power is 0) increases the RMSE substantially.

$$\hat{\rho}(t) = a_0 + a_1 \sin\frac{2\pi}{T}t + b_1 \cos\frac{2\pi}{T}t + c_2 e^{-n \cdot wv(t)} \quad (1)$$

where,

$\hat{\rho}$ is predicted Cirrus Band TOA reflectance,

t is Julian date,

T is the number of days per year ($T = 365.25$),

a_0 is coefficient for overall Cirrus Band TOA reflectance,

a_1, b_1 are coefficients for inter-annual change in the Cirrus Band (particularly useful in dry air environments),

c_2 is the coefficient for the water vapor deviation from what is normal,

wv is integrated water vapor (unit: kg/m^2),

n is equal to 1.

Fig. 6 shows two examples of the Cmask time series model. For the location with moist air (Fig. 6a), there is sufficient water vapor in the atmosphere and the Cirrus Band is dark consistently unless cirrus clouds (e.g., P2, P3, and P4) are present. The constant coefficient (a_0) is the most important factor for this simple environment and at the same time the remaining three coefficients (a_1, b_1, and c_2) are very close to zero. For the location with dry air (Fig. 6b), however, the atmospheric water vapor is less sufficient, and the Cirrus Band shows a seasonal pattern. The single constant coefficient (a_0) does not work, and the harmonic coefficients (a_1, b_1) are able to capture the intra-annual change, but cannot model the abnormal deviations in the Cirrus Band caused by rapid changes of the atmospheric water vapor content such as P4 and P5 in Fig. 6b. Fortunately, this kind of change can be captured by the water vapor variable (c_2), and the full model with all three coefficients (a_0, a_1, b_1, *and* c_2) achieves the best results (Fig. 6b). The benefits from the inclusion of the water vapor are also evidenced from Fig. 5, in which exclusion of water vapor would result in less accurate prediction of the Cirrus Band (larger RMSE). At the same time, by comparing the detected results using the model with water vapor and without water vapor, we observed a decrease in overall accuracy when the water vapor component is not included, and for places with dramatic water

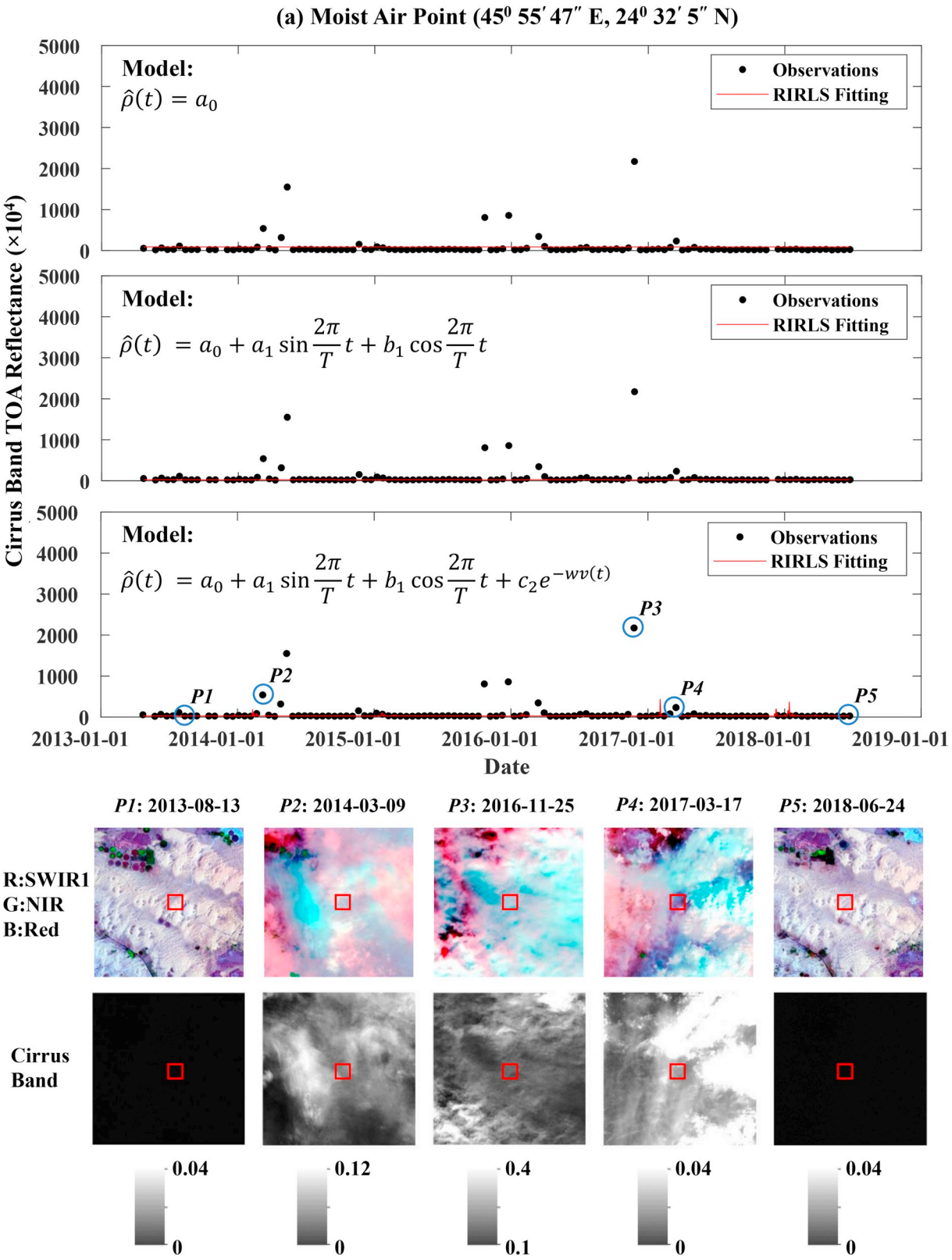

Fig. 6. Illustration of the different components of the Cmask time series model. (a) An example in a location characterized by moist air conditions. Observations P1 and P5 are clear while P2, P3, and P4 are affected by cirrus cloud. (b) An example in a location with dry air conditions. P1, P4, and P5 are clear observations while P2 and P3 are affected by cirrus cloud. Note all Landsat 8 Cirrus Band TOA reflectance data between March 2013 to June 2018 were used to generate the time series models using the Robust Iteratively Reweighted Least Squares (RIRLS) regression method (see Section 4.2 for details). The three time series plots in the upper panel illustrate the importance of the different components of the time series model, and the two rows of images in the lower panel show the Landsat 8 subset images collected at different points of time (first row – false color images with SWIR1, NIR, and Red Bands composited; second row – Cirrus Band TOA reflectance). The blue circles indicate the observations selected from the central pixel of the subset images in the lower panel. (For interpretation of the references to color in this figure legend, the reader is referred to the web version of this article.)

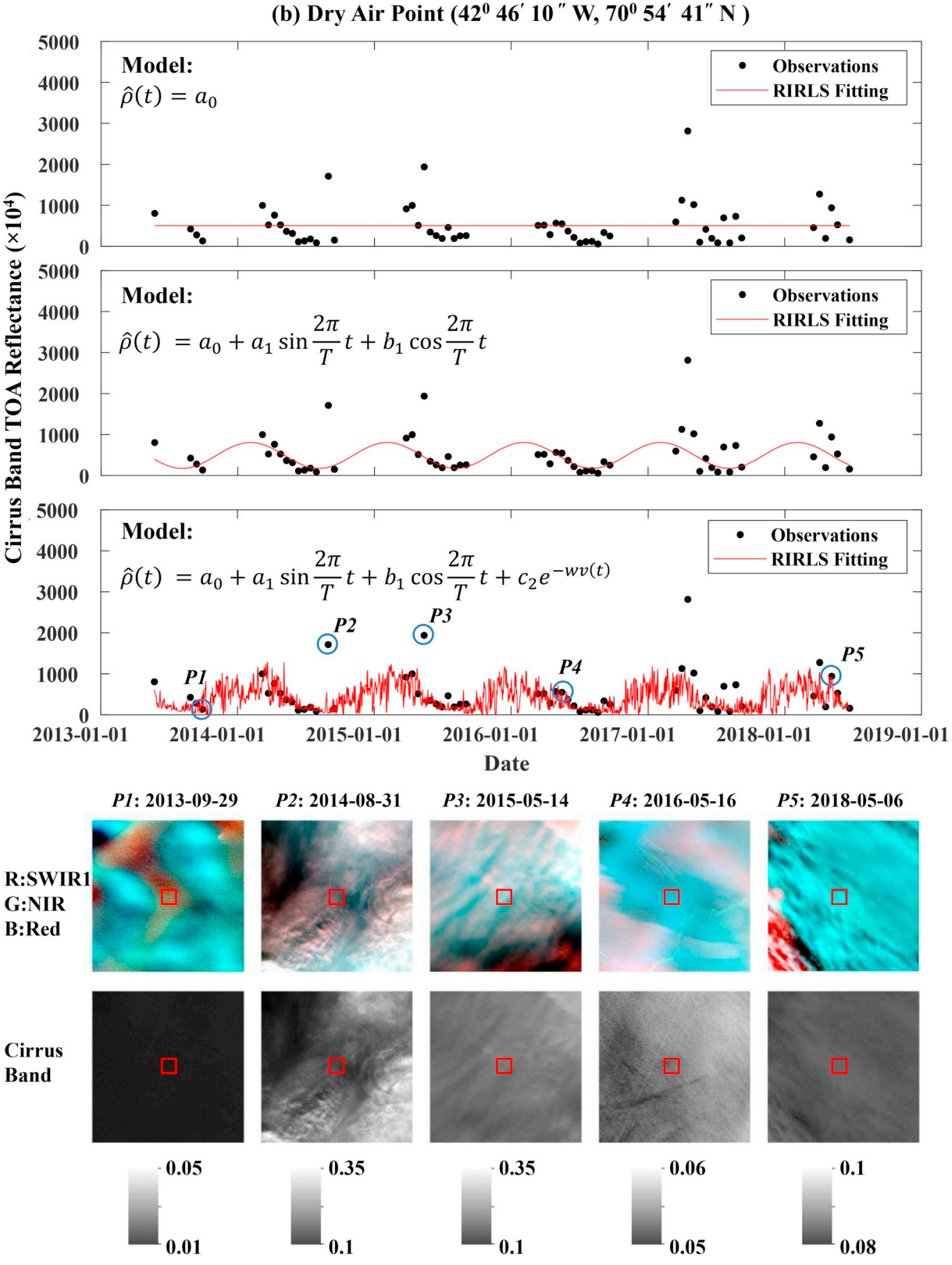

Fig. 6. (*continued*)

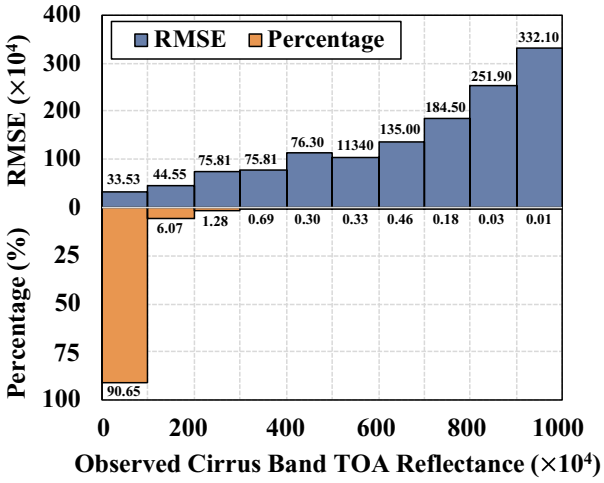

Fig. 7. Prediction accuracy of Cirrus Band TOA reflectance at different intervals of the observed Landsat Cirrus Band TOA reflectance based on 303 fully clear images. Prediction accuracy decreases along with the increments of the observed Cirrus Band. RMSE: Root Mean Square Error.

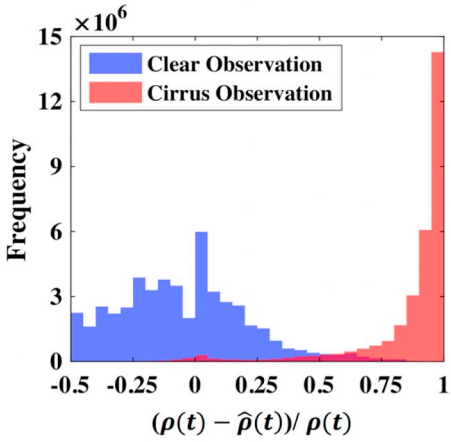

Fig. 9. Histogram of the normalized difference between observed and predicted Cirrus Band TOA reflectance for clear and cirrus cloud observations derived from the 303 clear images and 122 cirrus images. The value of 0.5 is optimal for distinguishing cirrus clouds from clear observations.

vapor changes, large commission of cirrus clouds were observed (see Section 5 for details).

4.2. Time series model estimation

For each pixel, Cmask estimates the coefficients of the time series model (Eq. (1)) based on all Landsat 8 Cirrus Band TOA reflectance data using the Robust Iteratively Reweighted Least Squares (RIRLS) regression approach (see Supplementary Materials for details). In each iteration, RIRLS can adjust the weights of each data point, which can greatly reduce and even remove the influence of outliers in the regression (Dumouchel and O'Brien, 1992; Heiberger and Becker, 1992; Holland and Welsch, 1977; O'Leary, 1990; Street et al., 1988). Considering the relatively infrequent occurrence of cirrus clouds (~20% globally) (Heymsfield et al., 2016; Kovalskyy and Roy, 2015), RIRLS can automatically exclude the limited number of outliers due to cirrus clouds, and use the remaining "good" observations to create the Cmask time series model.

We compared model predictions with real observations for the previously selected 303 clear images, and found that most of the predictions (more than 90%) are accurate (an average RMSE of 0.0034) (Fig. 7). On the other hand, we found the prediction accuracy decreases as Cirrus Band TOA reflectance increases (Fig. 7). The visual comparisons in Fig. 8a indicates that the predicted Cirrus Band is very similar to the observed Cirrus Band when the atmosphere is moist and the

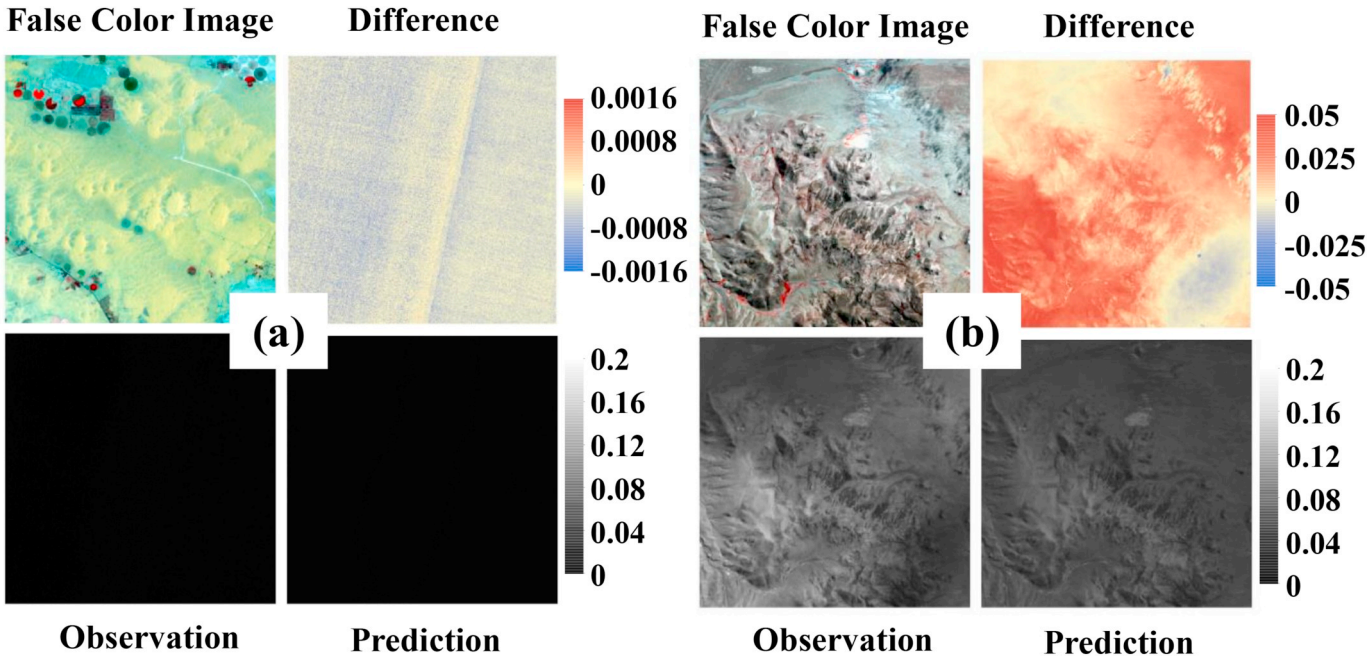

Fig. 8. Examples of Cmask predicted Cirrus Band TOA reflectance. (a) Results for the Landsat 8 image (Path 166/Row 43; May 28, 2014) where the air is moist and the Cirrus Band is relatively dark. (b) Results for the Landsat 8 image (Path 63/Row 15; March 7, 2014) where the air is relatively dry in the mountains. The images are central subset images of 500 pixels × 500 pixels from the original Landsat images. A false color image is shown with NIR, Red, and Green Bands composited. The difference image is calculated based on the observed Cirrus Band TOA reflectance minus the predicted Cirrus Band TOA reflectance. Note that the observed and predicted Cirrus bands are displayed using the same stretch, so they are directly comparable. (For interpretation of the references to color in this figure legend, the reader is referred to the web version of this article.)

Cirrus Band is dark. However, when the air is dry and the Cirrus Band includes a bright surface signal, the Cmask prediction is less accurate (see the high mountain areas in Fig. 8b).

4.3. Cirrus cloud detection

The main idea of cirrus cloud detection algorithm is based on the difference between the observed Cirrus Band TOA reflectance (ρ) and the predicted Cirrus Band TOA reflectance ($\hat{\rho}$). Ideally, the larger the difference ($\rho - \hat{\rho}$), the more likely it is a cirrus cloud observation. However, for places with high Cirrus Band TOA reflectance (e.g., high mountain and polar regions) this hypothesis may be no longer valid, as it is more difficult to predict the values of Cirrus Band TOA reflectance, and this problem is more severe when the observation value (ρ) increases (Fig. 7). Therefore, we used ρ to normalize the difference ($\rho - \hat{\rho}$) in Eq. (2), which magnifies the threshold to remove or sufficiently reduce the potential commission errors. For real cirrus clouds, this normalized difference will be close to 1, as ρ will be much larger than $\hat{\rho}$. For non-cirrus observations (including non-cirrus cloud and clear observations), the normalized difference will be close to zero or negative. To determine a threshold to detect cirrus clouds, we calculated the normalized difference distribution of many clear and cirrus cloud pixels (from 303 clear images and 122 cirrus images in Section 2.2) and found that 0.5 is the optimal threshold with the least overlap between the two distributions (Fig. 9). Moreover, according to the impact of thin cirrus clouds in Table 2, a simple difference test ($\rho - \hat{\rho}$) > 0.0031 (inherited from SWIR1 Band) is added as another criterion for cirrus cloud detection (Eq. (2)).

$$\frac{\rho(t) - \hat{\rho}(t)}{\rho(t)} > 0.5 \; and \; \frac{\rho(t) - \hat{\rho}(t)}{0.0031} > 1 \tag{2}$$

5. Visual and accuracy assessment

We compared the Cmask result with the cirrus cloud mask from the USGS QA Band visually and then assessed its accuracy.

5.1. Visual assessment

Compared with USGS QA, Cmask performs better in cirrus cloud

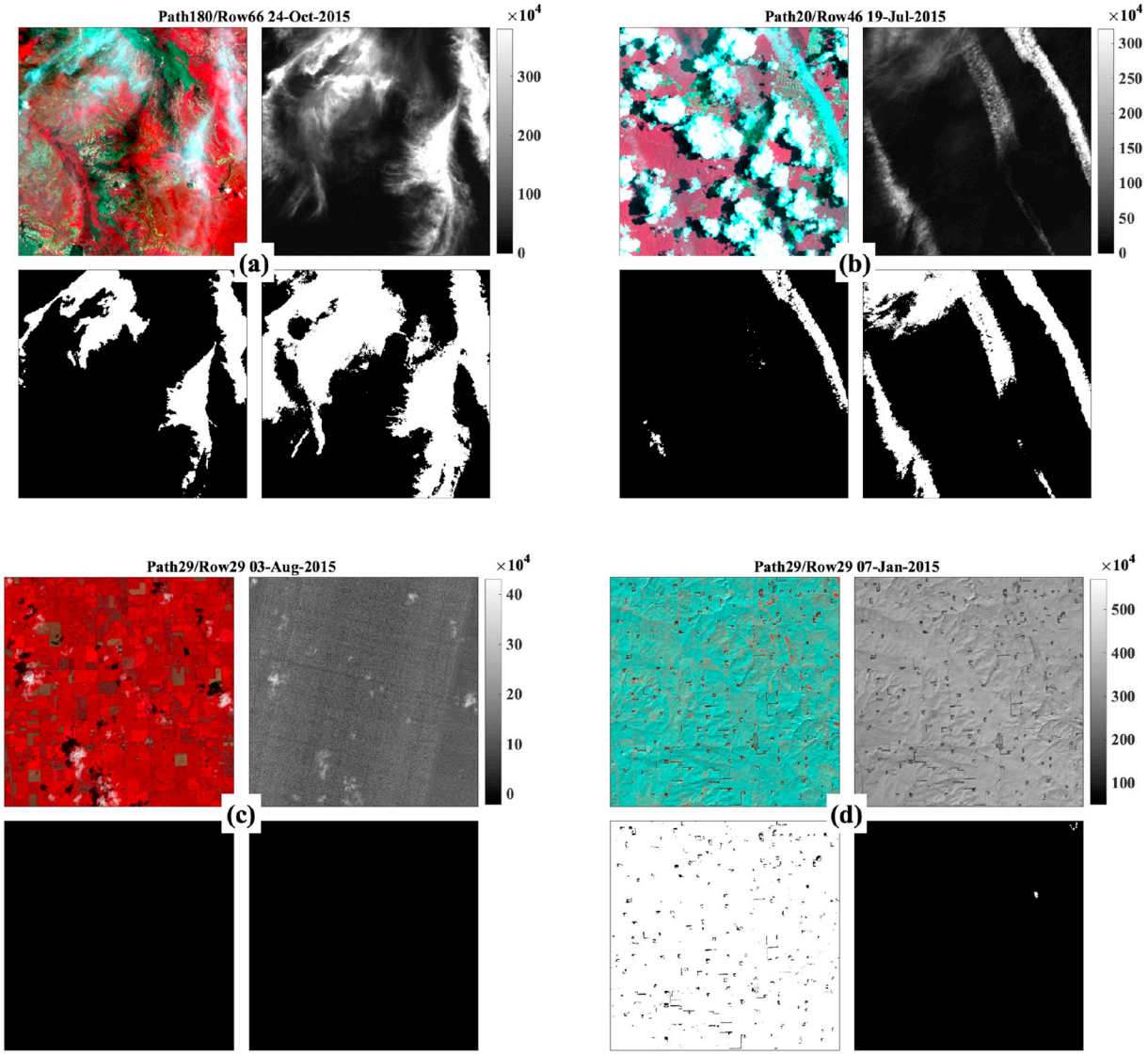

Fig. 10. Comparisons of Cmask and the USGS QA flag results (white color) for different Landsat images (subset images with 500 pixels × 500 pixels). The upper left image is a false color image. The upper right image is the Cirrus Band TOA reflectance (Unit: × 10^4). The lower left image is the USGS QA flag results. The lower right image is the Cmask results. The false color images in d, h, i, and j are shown with the SWIR1, NIR, and Red Bands composited, and the others are shown with the NIR, Red, and Green Bands composited. (For interpretation of the references to color in this figure legend, the reader is referred to the web version of this article.)

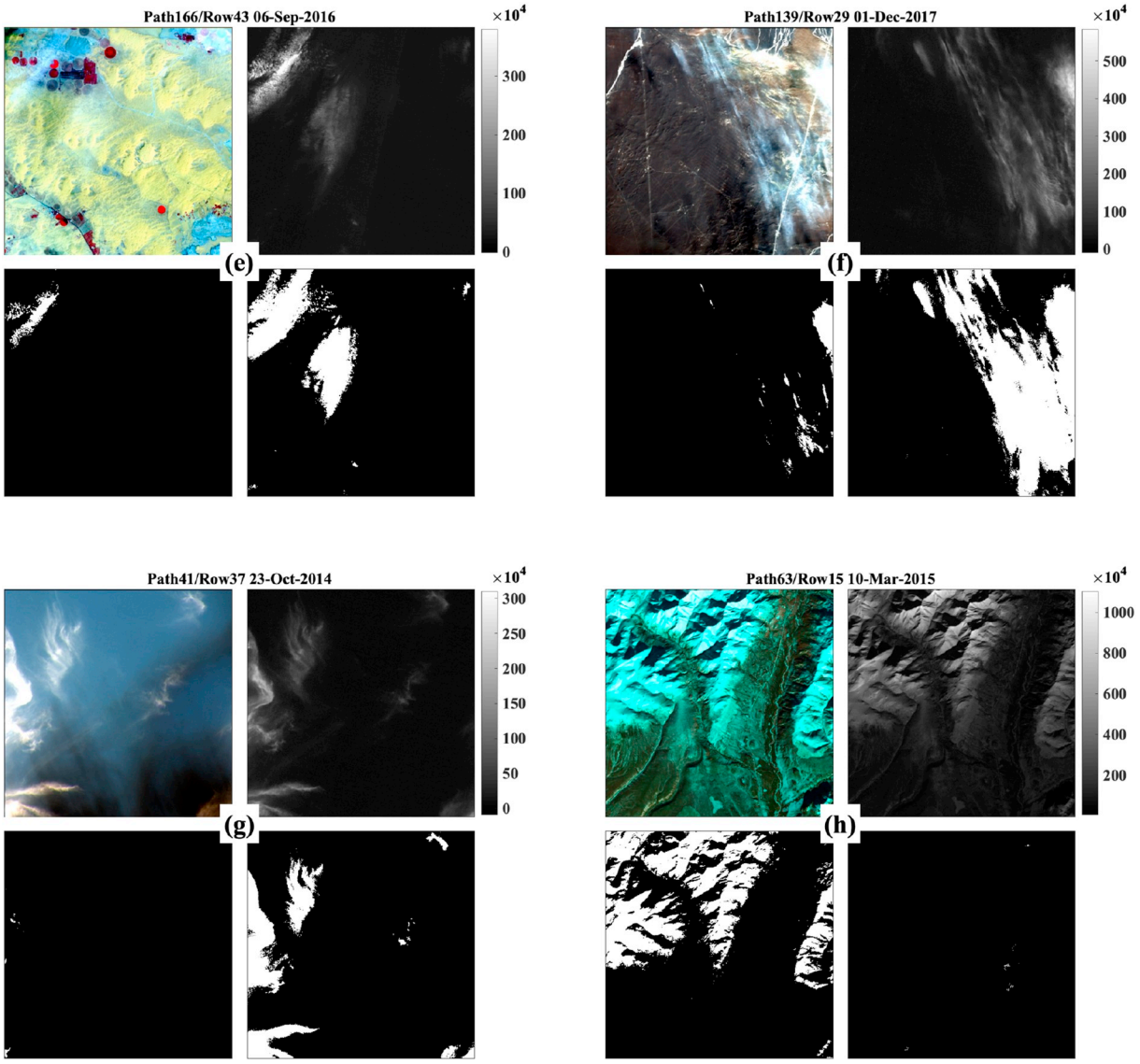

Fig. 10. (*continued*)

detection in different parts of the world (Fig. 10). Fig. 10a shows the results of a Landsat 8 image over a complex surface area of forest, barren, and water located in South-Central Africa, in which there are lots of thin cirrus clouds. Most of them are found by both Cmask and USGS QA, but the USGS QA data omits some cirrus clouds, especially at the boundaries of cirrus clouds. Fig. 10b shows a Landsat 8 image acquired from South American in tropical climates. There are lots of cumulus clouds and some cirrus clouds in this image. Compared to USGS QA, Cmask better detects the optically thin clouds. Fig. 10c and d show images characterized by agriculture from the same location in North American. In Fig. 10c, there are a few small cumulus clouds and a large area free of clouds. Both Cmask and USGS QA generated good cirrus cloud masks. For a different date (Fig. 10d), however, this area is covered by snow/ice and has high Cirrus Band TOA reflectance caused by the low water vapor in the atmosphere. For this special case, the USGS QA detected almost all of the clear surfaces as cirrus cloud, but Cmask did not have this problem. Fig. 10e shows an image in the Arabian Desert, characterized by some human activities (e.g., urban and agriculture). The USGS QA omitted thin cirrus clouds, but Cmask found them successfully. Fig. 10f illustrates the results of the image located in the Gobi Desert near Tibet. Comparing to the USGS QA, Cmask detected thin cirrus clouds more accurately. Fig. 10g shows a water image where Cmask successfully captured the thin cirrus clouds omitted in the USGS QA. Fig. 10h shows a mountainous image where snow/ice are present on the mountain tops. In the Cirrus Band, the high mountains (high reflectance) are apparent. The USGS QA flags show many commission errors in the high mountains, and Cmask works better in these situations. Fig. 10i and j share similar snow/ice coverage. The image in Fig. 10i is located in Greenland, when no cirrus clouds are present (there are some small cumulus clouds). The USGS QA flag misidentified the surface and the cumulus clouds as cirrus cloud. At the same time, it also omitted some cirrus clouds when snow/ice are present (Fig. 10j). Cmask showed better cirrus cloud detection results for the two images. More examples can be found in the Supplementary Materials (Pages 10–30).

5.2. Accuracy assessment

Compared with 'cirrus cloud' and 'non-cirrus' types from our validation samples (Table 1), Cmask achieved an overall accuracy of 86.41% at the pixel level, which is higher than USGS QA (83.28%) (Table 3). For identifying the cirrus clouds, the producer's accuracy of Cmask is 10% higher than that of USGS QA and the user's accuracy of Cmask is also higher than that of USGS QA (71.73% versus 67.77%).

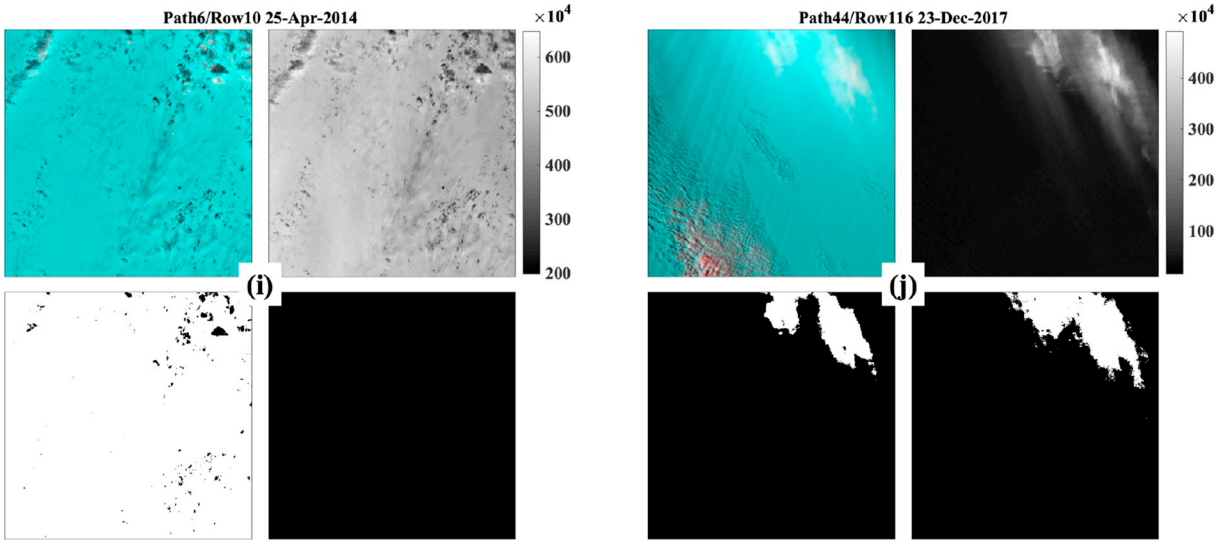

Fig. 10. (*continued*)

Table 3
Confusion matrix of comparison between Cmask and USGS QA for 'cirrus cloud' and 'non-cirrus'.

	Visual		User's (%)
	Cirrus cloud	Non-cirrus	
Cmask			
Cirrus cloud	373	147	71.73
Non-cirrus	87	1115	92.76
Producer's (%)	81.09	88.35	**Overall (%) 86.41**
USGS QA			
Cirrus cloud	328	156	67.77
Non-cirrus	132	1106	89.34
Producer's (%)	71.30	87.64	**Overall (%) 83.28**

Note 'non-cirrus' includes clear and any clouds type but not cirrus cloud.

Table 4
Confusion matrix of the comparison between Cmask and USGS QA for 'cirrus cloud' and 'clear'.

	Visual		User's (%)
	Cirrus cloud	Clear	
Cmask			
Cirrus cloud	373	23	94.19
Clear	87	853	90.74
Producer's (%)	81.09	97.37	**Overall (%) 91.77**
USGS QA			
Cirrus cloud	328	62	84.10
Clear	132	814	86.05
Producer's (%)	71.30	92.92	**Overall (%) 85.48**

Compared to USGS QA, Cmask also has higher producer's and user's accuracy for determining 'non-cirrus'.

Though Cmask is designed for detecting cirrus clouds solely, other non-cirrus clouds at high altitudes (e.g., top of cumulus cloud) are consistently labeled as cirrus clouds and are the major source of commission errors (Fig. 11). Considering that any kind of clouds need to be excluded for further applications, this kind of commission error is not particularly harmful. Therefore, we performed another accuracy assessment by excluding the reference samples for non-cirrus clouds and only considering the performance for distinguishing 'cirrus cloud' and 'clear' (Table 4). This adjusted accuracy assessment shows that the Cmask algorithm achieved a much higher overall accuracy than the USGA QA (91.77% versus 85.48%). For both producer's and user's accuracy for 'cirrus cloud', Cmask achieved approximately 10% higher accuracies than USGS QA in cirrus cloud detection and 5% ~ 6%

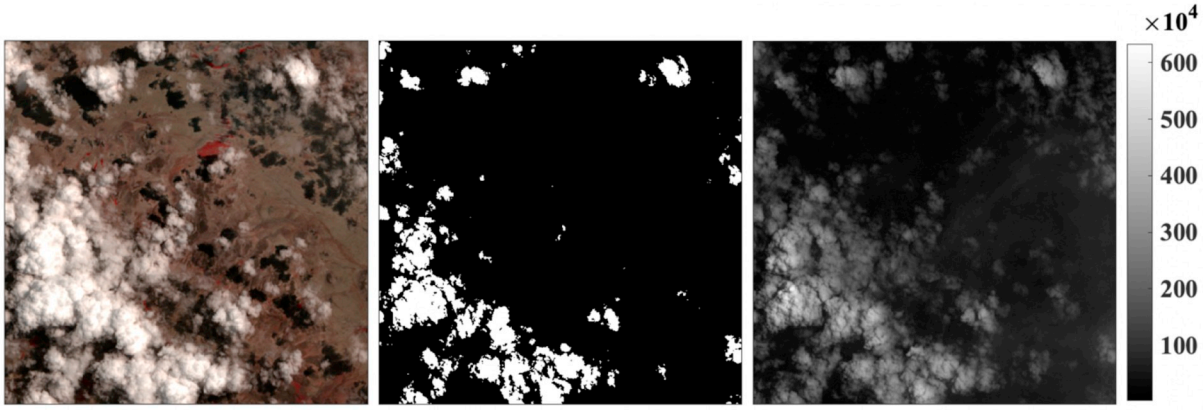

Fig. 11. An example of commission of cirrus clouds from non-cirrus clouds in Cmask for a Landsat 8 image with 500 pixels × 500 pixels located at Path 1/Row 73 acquired on March 13, 2017. Non-cirrus clouds located at high altitudes (e.g., top of cumulus cloud) were incorrectly masked as cirrus. The left image is the false color image shown with NIR, Red, and Green Bands composited. The middle image is the Cmask cirrus cloud mask (white color). The right image is the Cirrus Band TOA reflectance (Unit: × 10^4). (For interpretation of the references to color in this figure legend, the reader is referred to the web version of this article.)

improvements in producer's and user's accuracies than USGS QA for 'clear'. This means Cmask can reduce almost half errors compared to USGS QA (8% versus 15% of the total existing error).

6. Discussion and conclusions

In this study, we focused on the question 'what is a cirrus cloud in Landsat 8 imagery?' by quantitively comparing the increment of Cirrus Band TOA reflectance and the increment of optical band surface reflectance. We found that the impact of cirrus cloud is band-dependent and the surface reflectance of Blue Band is affected by cirrus cloud most seriously while the SWIR2 Band is the least influenced (Fig. 3 and Table 2). This is also similar to the findings in the studies made by DeSlover et al. (1999) and Gao and Li (2017). Based on the Landsat 8 surface reflectance product created by the LaSRC algorithm (Vermote et al., 2016), we empirically made a cirrus cloud definition that a pixel should be labeled as cirrus cloud when its Cirrus Band TOA reflectance increases 0.0031. This threshold is derived from atmospheric correction uncertainty in the SWIR1 Band, and users can also select another threshold from Table 2 to define how 'cirrus' a pixel should be identified, dependent on other optical band(s). It should be also noted that the cirrus cloud definition may change if another atmospheric correction method is used.

To answer the question 'how to accurately detect cirrus clouds in Landsat 8 images?', we proposed the Cmask algorithm by using the time series of the Cirrus Band and an external water vapor regressor. Benefiting from many observations in the Cirrus Band, Cmask is almost unaffected by surface reflectance, particularly in moist air conditions (sufficient water vapor). For example, there is a pixel changed from 'forest' to 'developed'. Although we can see the change from the optical bands such as Blue and SWIR1 (Fig. 12a and b), the Cirrus Band is still stable at low values due to water vapor absorption (Fig. 12c).

The inclusion of water vapor in the regression is important for improving cirrus cloud detection, particularly over areas with dry air, such as high mountains and polar ice/snow regions. By comparing Cmask results generated with and without water vapor regressor (Eq. (1)), we observed an overall 3.63% disagreement for all 2169 images, in which most of the images presented relatively small differences but some of them show large differences (Fig. 13). To evaluate the benefit of using water vapor regressor, we randomly created and manually interpreted 69 samples (including 'cirrus' and 'clear') at these places of disagreement. We found that Cmask using the water vapor regressor achieved much higher overall accuracy than when the water vapor regressor is omitted (75% versus 25%) (Table S4). This is mainly because the commission errors of 'cirrus cloud' from 'clear' substantially increase over the places with dramatic water vapor changes once the water vapor regressor is excluded (Fig. 14; Table S4). Therefore, we generally recommend including the water vapor regressor in the Cmask model, as it does no harm to the algorithm, and for places with dry

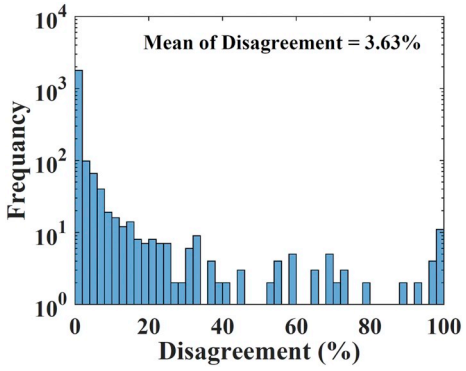

Fig. 13. Histogram of disagreements between Cmask with and without water vapor regressor for all 2169 images. The y-axis is at a log-10 scale.

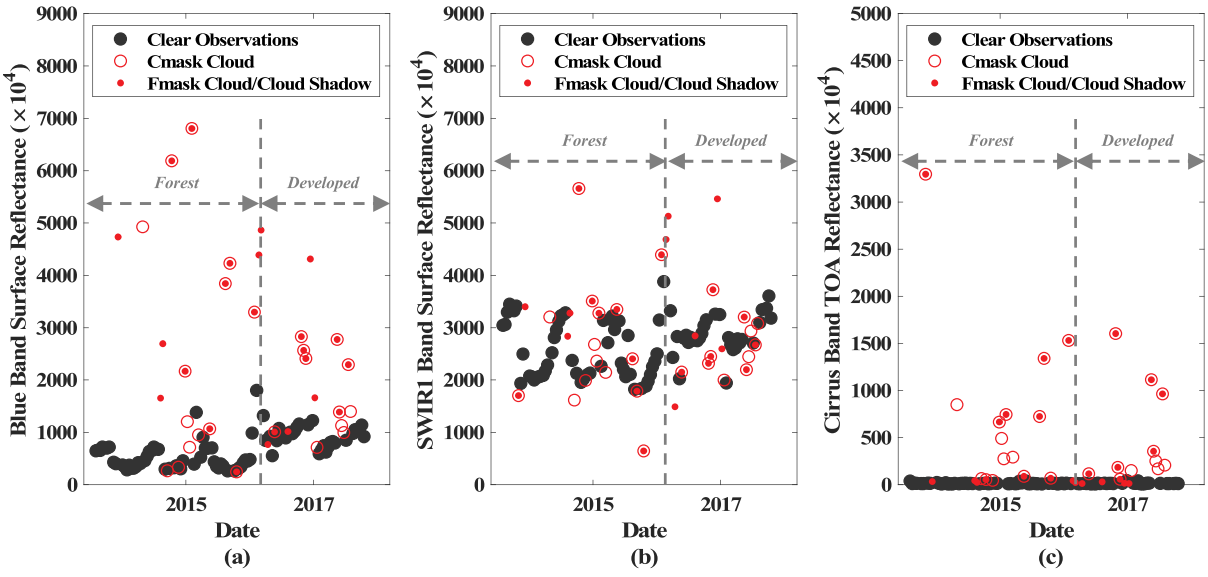

Fig. 12. Combination of Cmask and Fmask results for screening out clouds and cloud shadows for creating better Landsat 8 time series for a pixel located at 107° 20′ 58″ W, 24° 50′ 46″ N. (a) Time series of Blue Band surface reflectance. (b) Time series of SWIR1 Band surface reflectance. (c) Time series of Cirrus Band TOA reflectance. This pixel is changed from forest to developed. (For interpretation of the references to color in this figure legend, the reader is referred to the web version of this article.)

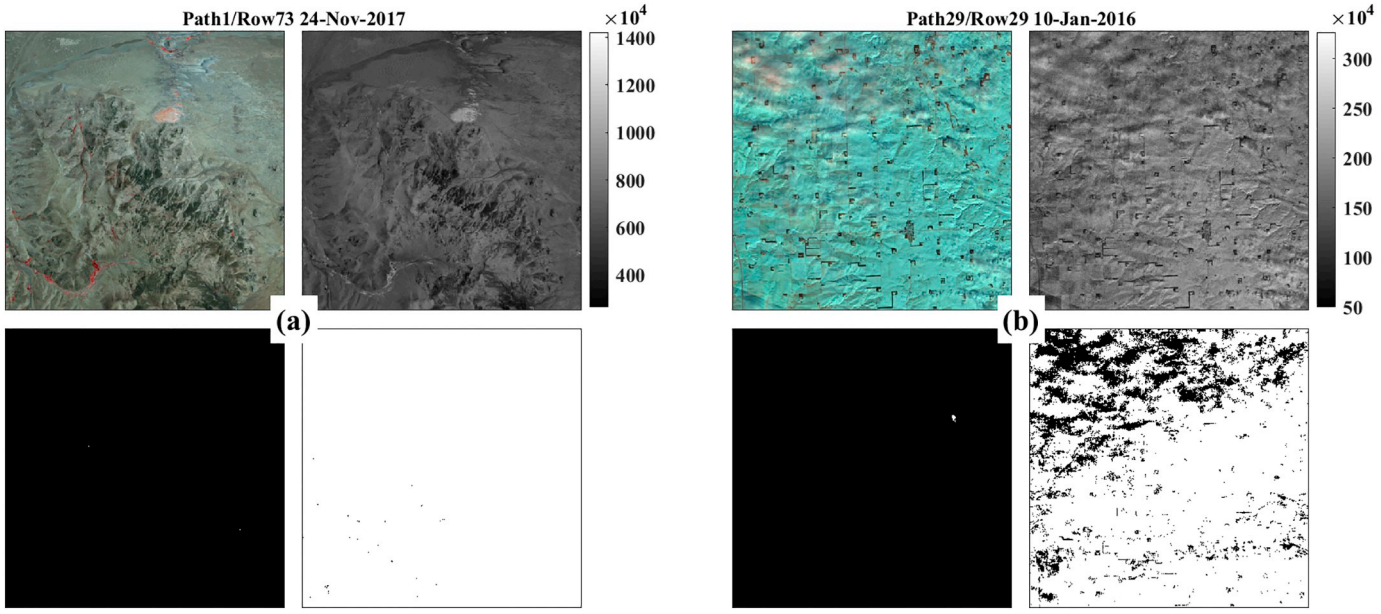

Fig. 14. Comparisons of Cmask result with and without water vapor regressor over high mountain (a) and snow/ice sheet (b). Almost all clear pixels are misidentified as cirrus cloud if water vapor regressor is excluded (Eq. (1)). Note that the upper left image is a false color image (a) shown with NIR, Red, and Green Bands composited, and (b) is shown with SWIR1, NIR, and Red Bands composited. The upper right image is the Cirrus Band TOA reflectance (Unit: × 10^4). The lower left image is the Cmask results with water vapor regressor. The lower right image is the Cmask results without water vapor regressor. White color indicates the presence of cirrus clouds. (For interpretation of the references to color in this figure legend, the reader is referred to the web version of this article.)

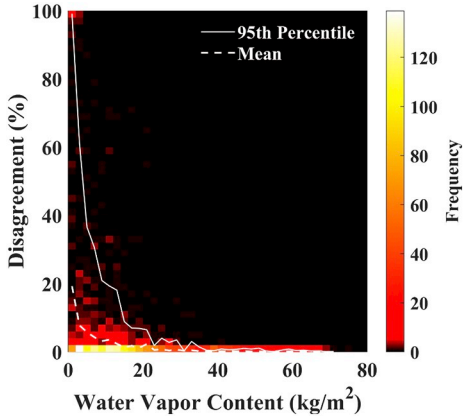

Fig. 15. Scatter plot of disagreement versus water vapor content for 2169 images. The disagreement generally increases as the water vapor content decreases. The mean disagreement will be larger than 2% with a maximum value (at 95th percentile) of 20% when the water vapor content is less than 10 kg/m^2. Disagreement indicates the places where Cmask with and Cmask without water vapor regressor do not agree. The 95th percentile and the mean lines are calculated based on the data in each water vapor bin with an interval of 2 kg/m^2.

atmospheric conditions this extra component will greatly improve Cmask algorithm by reducing commission errors. The water vapor data we used are from global MERRA-2 reanalysis data with coarser spatial resolution, and outliers are sometimes present, particularly in high latitudes (Gelaro et al., 2017). If a better global water vapor product free of clouds can be acquired, the Cmask algorithm will work better.

To evaluate the impacts of water vapor on Cmask, we plot the percent of disagreement (Cmask results with versus without using water vapor regressor) against the water vapor content for all the 2169 images (Fig. 15). It is clear that the lower the water vapor content the larger the percent of disagreement. It is worth noting that when the water vapor content is larger than 10 kg/m^2, the mean disagreement is less than 2%, and majority of the disagreements (95th percentile) are less than 20%, which indicates water vapor regressor has very limited effect on Cmask with water vapor content at this level. Therefore, we can create a global mask of places where water vapor regressor should be included in Cmask if their historical lowest water vapor content is less than 10 kg/m^2, and in the other places water vapor regressor is optional (Fig. 16).

Additionally, Cmask detects some non-cirrus clouds located at high altitudes (e.g., cumulus overshooting top) as well (Fig. 11). This is not a problem for a cloud detection algorithm because any kind of cloud should be screened out for further applications (e.g., land cover change detection) (Bullock et al., 2019; Huang et al., 2009; Zhu et al., 2012). At the same time, considering that Cmask is not designed for detecting non-cirrus clouds, we recommend combining Cmask and another cloud detection algorithm (e.g., Fmask) to detect all kinds of clouds in LTS. In Fig. 12, an observation is labeled as clear if both Fmask and Cmask detect them as clear (black dots). Although Cmask is designed for Landsat 8, it can be easily transferred to any sensor with a cirrus band (e.g., Sentinel-2).

Cmask also has some limitations. First, it may misidentify some clear surfaces as cirrus cloud, such as in high mountain areas (Fig. 17a). This occurs because Cmask may underestimate the Cirrus Band. Though some commission errors may occur in high reflectance areas, we observed that only very few images have this problem. Second, Cmask had some omission errors of cirrus cloud, especially in high cirrus TOA reflectance areas such as polar regions (Fig. 17b). The omission errors are mainly from very thin cirrus clouds, because the observation-corrected difference makes Cmask require a higher threshold to detect cirrus cloud (Eq. (2)), but the thin cirrus clouds only brighten the Cirrus Band by a small amount especially for very bright surfaces (e.g., snow/ice). Considering very few cirrus clouds are over those places (Sassen et al., 2008) this is not a serious issue. The users can also increase or decrease the detection threshold to reduce the commission or the omission errors for their study areas and research purposes (Eq. (2); Fig. 9).

In conclusion, we provided a quantitive definition of when a pixel should be labeled as ‘cirrus cloud’ and proposed a new cloud detection algorithm called Cmask for operational and automated detection of

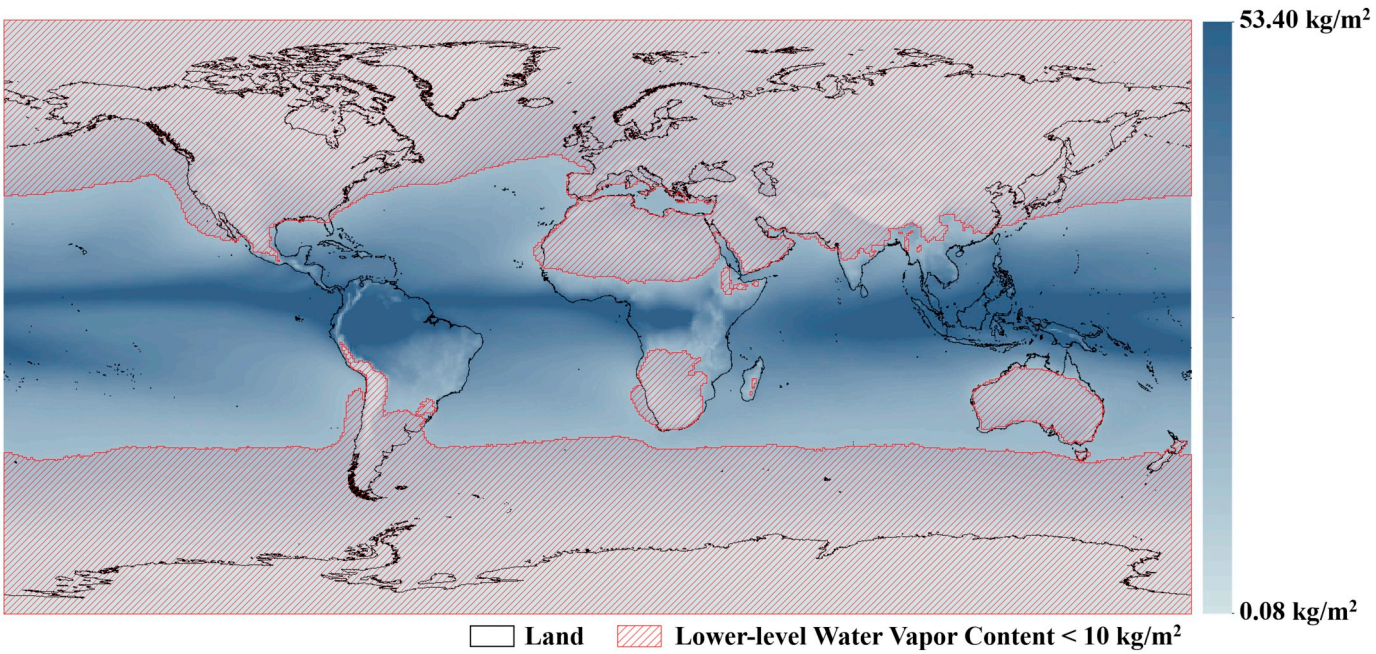

Fig. 16. Global mask of places where water vapor regressor should be included in Cmask (red mask). Minimum water vapor content is the background. The minimum values of global water vapor content are calculated based on historical daily water vapor products from MERRA-2 data between 2013 and 2017 at 5th percentile to exclude possible data errors. (For interpretation of the references to color in this figure legend, the reader is referred to the web version of this article.)

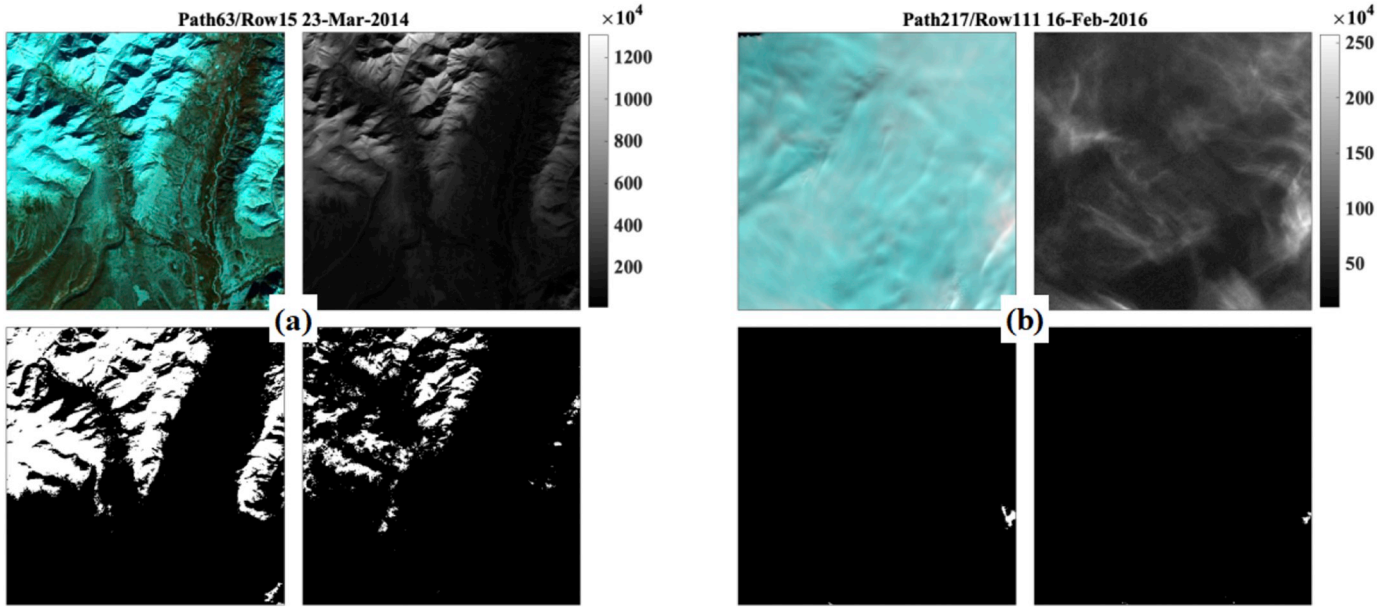

Fig. 17. Examples of Cmask commission (a) and omission (b) errors. The upper left image is the false color image shown with SWIR1, NIR, and Red Bands composited. The upper right image is the Cirrus Band TOA reflectance (Unit: $\times 10^4$). The lower left image is the cirrus cloud mask of USGS QA (white color). The lower right image is the cirrus cloud mask generated by Cmask (white color). (For interpretation of the references to color in this figure legend, the reader is referred to the web version of this article.)

cirrus clouds in Landsat 8 imagery. Cmask reduces almost by half the errors when distinguishing cirrus cloud and clear observations compared to the USGS QA (8% versus 15% in the total existing error).

Author statement

S.Q., Z.Z., and C.W. designed the study. S.Q. implemented the research and wrote the paper. Z.Z. and C.W. provided suggestions and edits for the paper.

Declaration of competing interest

The authors declare that they have no known competing financial interests or personal relationships that could have appeared to influence the work reported in this paper.

Acknowledgments

The authors wish to thank USGS for providing the Landsat 8 cloud cover assessment dataset and three anonymous reviewers for insightful comments. This study was supported by USGS-NASA Landsat Science

Team (LST) Program for Toward Near Real-time Monitoring and Characterization of Land Surface Change for the Conterminous US (#140G0119C0008). The content of this document does not necessarily represent the views or policies of the Department of the Interior, nor does mention of trade names, commercial products or organizations imply endorsement by the U.S. Government.

Appendix A. Supplementary data

Supplementary data to this article can be found online at https://doi.org/10.1016/j.rse.2020.111884.

References

Ackerman, S.A., Strabala, K.I., Menzel, W.P., Frey, R.A., Moeller, C.C., Gumley, L.E., 1998. Discriminating clear sky from clouds with MODIS. J. Geophys. Res. Atmos. 103, 32141–32157. https://doi.org/10.1029/1998JD200032.

Brown, J.F., Tollerud, H.J., Barber, C.P., Zhou, Q., Dwyer, J.L., Vogelmann, J.E., Loveland, T.R., Woodcock, C.E., Stehman, S.V., Zhu, Z., Pengra, B.W., 2019. Lessons learned implementing an operational continuous United States national land change monitoring capability: the Land Change Monitoring, Assessment, and Project (LCMAP) approach. Remote Sens. Environ. https://doi.org/10.1016/j.rse.2019.111356. 111356.

Bullock, E.L., Woodcock, C.E., Holden, C.E., 2019. Improved change monitoring using an ensemble of time series algorithms. Remote Sens. Environ. https://doi.org/10.1016/j.rse.2019.04.018. 111165.

Burkhardt, U., Kärcher, B., 2011. Global radiative forcing from contrail cirrus. Nat. Clim. Chang. 1, 54–58.

Chai, D., Newsam, S., Zhang, H.K., Qiu, Y., Huang, J., 2019. Cloud and cloud shadow detection in Landsat imagery based on deep convolutional neural networks. Remote Sens. Environ. 225, 307–316. https://doi.org/10.1016/j.rse.2019.03.007.

Davis, J.C., 1986. Statistics and Data Analysis in Geology. Willey Sons, New York.

DeSlover, D.H., Smith, W.L., Piironen, P.K., Eloranta, E.W., 1999. A methodology for measuring cirrus cloud visible-to-infrared spectral optical depth ratios. J. Atmos. Ocean. Technol. 16, 251–262. https://doi.org/10.1175/1520-0426(1999)016<0251:AMFMCC>2.0.CO;2.

Dumouchel, W., O'Brien, F., 1992. Integrating a robust option into a multiple regression computing environment. In: Computing and Graphics in Statistics. Springer-Verlag New York, Inc., pp. 41–48.

Foga, S., Scaramuzza, P.L., Guo, S., Zhu, Z., Dilley, R.D., Beckmann, T., Schmidt, G.L., Dwyer, J.L., Joseph Hughes, M., Laue, B., 2017. Cloud detection algorithm comparison and validation for operational Landsat data products. Remote Sens. Environ. 194, 379–390. https://doi.org/10.1016/j.rse.2017.03.026.

Frantz, D., Röder, A., Udelhoven, T., Schmidt, M., 2015. Enhancing the detectability of clouds and their shadows in multitemporal dryland Landsat imagery: extending Fmask. IEEE Geosci. Remote Sens. Lett. 12, 1242–1246. https://doi.org/10.1109/LGRS.2015.2390673.

Frey, R.A., Ackerman, S.A., Liu, Y., Strabala, K.I., Zhang, H., Key, J.R., Wang, X., 2008. Cloud detection with MODIS. Part I: improvements in the MODIS cloud mask for collection 5. J. Atmos. Ocean. Technol. 25, 1057–1072. https://doi.org/10.1175/2008JTECHA1052.1.

Gao, B.C., Li, R.R., 2017. Removal of thin cirrus scattering effects in landsat 8 OLI images using the cirrus detecting channel. Remote Sens. 9, 1–10. https://doi.org/10.3390/rs9080834.

Gao, B.C., Goetz, A.F.H., Wiscombe, W.J., 1993. Cirrus cloud detection from airborne imaging spectrometer data using the 1.38 μm water vapor band. Geophys. Res. Lett. 20, 301–304. https://doi.org/10.1029/93GL00106.

Gao, B.C., Yang, P., Li, R.R., 2003. Detection of high clouds in polar regions during the daytime using the MODIS 1.375-/spl mu/m channel. IEEE Trans. Geosci. Remote Sens. 41, 474–481. https://doi.org/10.1109/Tgrs.2002.808290.

Gelaro, R., McCarty, W., Suárez, M.J., Todling, R., Molod, A., Takacs, L., Randles, C.A., Darmenov, A., Bosilovich, M.G., Reichle, R., Wargan, K., Coy, L., Cullather, R., Draper, C., Akella, S., Buchard, V., Conaty, A., da Silva, A.M., Gu, W., Kim, G.K., Koster, R., Lucchesi, R., Merkova, D., Nielsen, J.E., Partyka, G., Pawson, S., Putman, W., Rienecker, M., Schubert, S.D., Sienkiewicz, M., Zhao, B., 2017. The modern-era retrospective analysis for research and applications, version 2 (MERRA-2). J. Clim. 30, 5419–5454. https://doi.org/10.1175/JCLI-D-16-0758.1.

GMAO, 2015. MERRA-2 inst1_2d_int_Nx: 2d,1-Hourly, Instantaneous,Single-Level, Assimilation, Vertically Integrated Diagnostics V5.12.4 [Dataset]. NASA's Goddard Earth Sci. Data Inf. Serv. Cent. (GES DISC)$32#https://doi.org/10.5067/G0U6NGQ3BLE0.

Goodwin, N.R., Collett, L.J., Denham, R.J., Flood, N., Tindall, D., 2013. Cloud and cloud shadow screening across Queensland, Australia: an automated method for Landsat TM/ETM+ time series. Remote Sens. Environ. 134, 50–65. https://doi.org/10.1016/j.rse.2013.02.019.

Guenther, B., Xiong, X., Salomonson, V., Barnes, W., Young, J., 2002. On-orbit performance of the earth observing system moderate resolution imaging spectroradiometer; first year of data. Remote Sens. Environ. 83, 16–30. https://doi.org/10.1016/S0034-4257(02)00097-4.

Hagolle, O., Huc, M., Pascual, D.V., Dedieu, G., 2010. A multi-temporal method for cloud detection, applied to FORMOSAT-2, VENμS, LANDSAT and SENTINEL-2 images. Remote Sens. Environ. 114, 1747–1755. https://doi.org/10.1016/j.rse.2010.03.002.

Hansen, M.C., Potapov, P.V., Moore, R., Hancher, M., Turubanova, S.A.A., Tyukavina, A., Thau, D., Stehman, S.V., Goetz, S.J., Loveland, T.R., Kommareddy, A., 2013. High-resolution global maps of 21st-century forest cover change. Science (80-.) 342, 850–853. https://doi.org/10.1126/science.1244693.

Heiberger, R.M., Becker, R.A., 1992. Design of an S function for robust regression using iteratively reweighted least squares. J. Comput. Graph. Stat. 1, 181–196.

Heymsfield, A.J., Krämer, M., Luebke, A., Brown, P., Cziczo, D.J., Franklin, C., Lawson, P., Lohmann, U., McFarquhar, G., Ulanowski, Z., Van Tricht, K., 2016. Cirrus clouds. In: Meteorological Monographs, https://doi.org/10.1175/amsmonographs-d-16-0010.1. 2.1-2.26.

Holden, C.E., Woodcock, C.E., 2016. An analysis of Landsat 7 and Landsat 8 underflight data and the implications for time series investigations. Remote Sens. Environ. 185, 16–36. https://doi.org/10.1016/j.rse.2016.02.052.

Holland, P.W., Welsch, R.E., 1977. Robust regression using iteratively reweighted least-squares. Commun. Stat. Methods 6, 813–827.

Huang, C., Goward, S.N., Masek, J.G., Gao, F., Vermote, E.F., Thomas, N., Schleeweis, K., Kennedy, R.E., Zhu, Z., Eidenshink, J.C., Townshend, J.R.G., 2009. Development of time series stacks of landsat images for reconstructing forest disturbance history. Int. J. Digit. Earth 2, 195–218. https://doi.org/10.1080/17538940902801614.

Huang, C., Goward, S.N., Masek, J.G., Thomas, N., Zhu, Z., Vogelmann, J.E., 2010a. An automated approach for reconstructing recent forest disturbance history using dense Landsat time series stacks. Remote Sens. Environ. 114, 183–198. https://doi.org/10.1016/j.rse.2009.08.017.

Huang, C., Thomas, N., Goward, S.N., Masek, J.G., Zhu, Z., Townshend, J.R.G., Vogelmann, J.E., 2010b. Automated masking of cloud and cloud shadow for forest change analysis using Landsat images. Int. J. Remote Sens. 31, 5449–5464. https://doi.org/10.1080/01431160903369642.

Huschke, R.E., 1970. Glossary of Meteorology. American Meteorological Society, Boston, MA.

Irish, R.R., Barker, J.L., Goward, S.N., Arvidson, T., 2006. Characterization of the Landsat-7 ETM+ Automated Cloud-Cover Assessment (ACCA) Algorithm. Photogramm. Eng. Remote. Sens. 72, 1179–1188. https://doi.org/10.14358/PERS.72.10.1179.

Kennedy, R.E., Yang, Z., Cohen, W.B., 2010. Detecting trends in forest disturbance and recovery using yearly Landsat time series: 1. LandTrendr—Temporal segmentation algorithms. Remote Sens. Environ. 114, 2897–2910. https://doi.org/10.1016/j.rse.2010.07.008.

King, M.D., et al., 2003. Cloud and aerosol properties, precipitable water, and profiles of temperature and water vapor from MODIS. IEEE Trans. Geosci. Remote Sens. 41, 442–458. https://doi.org/10.1109/TGRS.2002.808226.

Kovalskyy, V., Roy, D.P., 2015. A one year Landsat 8 conterminous United States study of cirrus and non-cirrus clouds. Remote Sens. 7, 564–578. https://doi.org/10.3390/rs70100564.

Loveland, T.R., Reed, B.C., Ohlen, D.O., Brown, J.F., Zhu, Z., Yang, L., Merchant, J.W., 2000. Development of a global land cover characteristics database and IGBP DISCover from 1 km AVHRR data. Int. J. Remote Sens. 21, 1303–1330. https://doi.org/10.1080/014311600210191.

Luo, Y., Trishchenko, A.P., Khlopenkov, K.V., 2008. Developing clear-sky, cloud and cloud shadow mask for producing clear-sky composites at 250-meter spatial resolution for the seven MODIS land bands over Canada and North America. Remote Sens. Environ. 112, 4167–4185. https://doi.org/10.1016/j.rse.2008.06.010.

Mace, G.G., Clothiaux, E.E., Ackerman, T.P., Mace, G.G., Clothiaux, E.E., Ackerman, T.P., 2001. The composite characteristics of cirrus clouds: bulk properties revealed by one year of continuous cloud radar data. J. Clim. 14, 2185–2203. https://doi.org/10.1175/1520-0442(2001)014<2185:TCCOCC>2.0.CO;2.

Mastenbrook, H.J., 1971. The variability of water vapor in the stratosphere. J. Atmos. Sci. 28, 1495–1501. https://doi.org/10.1175/1520-0469(1971)028<1495:tvowvi>2.0.co;2.

Nilsson, T., Elgered, G., 2008. Long-term trends in the atmospheric water vapor content estimated from ground-based GPS data. J. Geophys. Res. Atmos. 113. https://doi.org/10.1029/2008JD010110.

O'Leary, D.P., 1990. Robust regression computation using iteratively reweighted least squares. SIAM J. Matrix Anal. Appl. 11, 466–480.

Pekel, J.-F., Cottam, A., Gorelick, N., Belward, A.S., 2016. High-resolution mapping of global surface water and its long-term changes. Nature 540, 418–422. https://doi.org/10.1038/nature20584.

Platnick, S., King, M.D., Ackerman, S.A., Menzel, W.P., Baum, B.A., Riédi, J.C., Frey, R.A., 2003. The MODIS cloud products: algorithms and examples from terra. IEEE Trans. Geosci. Remote Sens. 41, 459–472. https://doi.org/10.1109/TGRS.2002.808301.

Qiu, S., Lin, Y., Shang, R., Zhang, J., Ma, L., Zhu, Z., Qiu, S., Lin, Y., Shang, R., Zhang, J., Ma, L., Zhu, Z., 2019a. Making landsat time series consistent: evaluating and improving landsat analysis ready data. Remote Sens. 11, 51. https://doi.org/10.3390/RS11010051.

Qiu, S., Zhu, Z., He, B., 2019b. Fmask 4.0: improved cloud and cloud shadow detection in Landsats 4–8 and Sentinel-2 imagery. Remote Sens. Environ. 231$32#https://doi.org/10.1016/j.rse.2019.05.024. 111205.

Rayner, J.N., 1971. Introduction to Spectral Analysis.

Sassen, K., Wang, Z., Liu, D., 2008. Global distribution of cirrus clouds from CloudSat/cloud-aerosol lidar and infrared pathfinder satellite observations (CALIPSO) measurements. J. Geophys. Res. Atmos. 113https://doi.org/10.1029/2008JD009972. D00A12.

Street, J.O., Carroll, R.J., Ruppert, D., 1988. A note on computing robust regression estimates via iteratively reweighted least squares. Am. Stat. 42, 152–154.

USGS, 2014. Landsat 8 Collection 1 Level-2 Scene Products (Surface Reflectance) [Dataset]. U.S. Geol. Surv. Earth Resour. Obs. Sci. Cent$32#https://doi.org/10.

5066/F78S4MZJ.
Vermote, E., Justice, C., Claverie, M., Franch, B., 2016. Preliminary analysis of the performance of the Landsat 8/OLI land surface reflectance product. Remote Sens. Environ. 185, 46–56. https://doi.org/10.1016/j.rse.2016.04.008.
Wilson, M.J., Oreopoulos, L., 2013. Enhancing a simple MODIS cloud mask algorithm for the landsat data continuity mission. IEEE Trans. Geosci. Remote Sens. 51, 723–731. https://doi.org/10.1109/TGRS.2012.2203823.
Woodcock, C.E., Allen, R., Anderson, M., Belward, A., Bindschadler, R., Cohen, W., Gao, F., Goward, S.N., Helder, D., Helmer, E., Nemani, R., Oreopoulos, L., Schott, J., Thenkabail, P.S., Vermote, E.F., Vogelmann, J., Wulder, M.A., Wynne, R., 2008. Free access to Landsat imagery. Science (80-.) 320https://doi.org/10.1126/science.320.5879.1011a. 1011.
Wulder, M.A., Loveland, T.R., Roy, D.P., Crawford, C.J., Masek, J.G., Woodcock, C.E., Allen, R.G., Anderson, M.C., Belward, A.S., Cohen, W.B., Dwyer, J., Erb, A., Gao, F., Griffiths, P., Helder, D., Hermosilla, T., Hipple, J.D., Hostert, P., Hughes, M.J., Huntington, J., Johnson, D.M., Kennedy, R., Kilic, A., Li, Z., Lymburner, L., McCorkel, J., Pahlevan, N., Scambos, T.A., Schaaf, C., Schott, J.R., Sheng, Y., Storey, J., Vermote, E., Vogelmann, J., White, J.C., Wynne, R.H., Zhu, Z., 2019. Current status of Landsat program, science, and applications. Remote Sens. Environ. 225, 127–147. https://doi.org/10.1016/j.rse.2019.02.015.
Zhu, X., Helmer, E.H., 2018. An automatic method for screening clouds and cloud shadows in optical satellite image time series in cloudy regions. Remote Sens. Environ. 214, 135–153. https://doi.org/10.1016/j.rse.2018.05.024.
Zhu, Z., Woodcock, C.E., 2012. Object-based cloud and cloud shadow detection in Landsat imagery. Remote Sens. Environ. 118, 83–94. https://doi.org/10.1016/j.rse.2011.10.028.
Zhu, Z., Woodcock, C.E., 2014a. Continuous change detection and classification of land cover using all available Landsat data. Remote Sens. Environ. 144, 152–171. https://doi.org/10.1016/j.rse.2014.01.011.
Zhu, Z., Woodcock, C.E., 2014b. Automated cloud, cloud shadow, and snow detection in multitemporal Landsat data: an algorithm designed specifically for monitoring land cover change. Remote Sens. Environ. 152, 217–234. https://doi.org/10.1016/j.rse.2014.06.012.
Zhu, Z., Woodcock, C.E., Olofsson, P., 2012. Continuous monitoring of forest disturbance using all available Landsat imagery. Remote Sens. Environ. 122, 75–91. https://doi.org/10.1016/j.rse.2011.10.030.
Zhu, Z., Wang, S., Woodcock, C.E., 2015a. Improvement and expansion of the Fmask algorithm: cloud, cloud shadow, and snow detection for Landsats 4-7, 8, and Sentinel 2 images. Remote Sens. Environ. 159, 269–277. https://doi.org/10.1016/j.rse.2014.12.014.
Zhu, Z., Woodcock, C.E., Holden, C., Yang, Z., 2015b. Generating synthetic Landsat images based on all available Landsat data: predicting Landsat surface reflectance at any given time. Remote Sens. Environ. 162, 67–83. https://doi.org/10.1016/j.rse.2015.02.009.
Zhu, Z., Qiu, S., He, B., Deng, C., 2018. Cloud and cloud shadow detection for Landsat images: the fundamental basis for analyzing Landsat time series. Remote Sens. Time Ser. Image Process. 3–24. https://doi.org/10.1201/9781315166636-10.
Zhu, Z., Wulder, M.A., Roy, D.P., Woodcock, C.E., Hansen, M.C., Radeloff, V.C., Healey, S.P., Schaaf, C., Hostert, P., Strobl, P., Pekel, J.F., Lymburner, L., Pahlevan, N., Scambos, T.A., 2019. Benefits of the free and open Landsat data policy. Remote Sens. Environ. 224, 382–385. https://doi.org/10.1016/j.rse.2019.02.016.